Deep-Sea Research I 116 (2016) 200–219

Contents lists available at ScienceDirect

Deep-Sea Research I

journal homepage: www.elsevier.com/locate/dsri

Biometric assessment of deep-sea vent megabenthic communities using multi-resolution 3D image reconstructions

Blair Thornton [a,b,*], Adrian Bodenmann [a], Oscar Pizarro [c], Stefan B. Williams [c], Ariell Friedman [d], Ryota Nakajima [e,f,1], Ken Takai [f], Kaori Motoki [f,g], Tomo-o Watsuji [f], Hisako Hirayama [f], Yohei Matsui [h], Hiromi Watanabe [e], Tamaki Ura [i]

[a] Institute of Industrial Science, The University of Tokyo, 4-6-1 Komaba, Meguro-ku, Tokyo 153-8505, Japan
[b] Southampton Marine and Maritime Institute, University of Southampton, Southampton SO16 7QF, UK
[c] Australian Centre for Field Robotics, The University of Sydney, NSW 2006, Australia
[d] Greybits, Sydney, NSW 2029, Australia
[e] Department of Marine Biodiversity Research, Japan Agency for Marine-Earth Science and Technology, Yokosuka, Kanagawa 237-0061, Japan
[f] Department of Subsurface Geobiological Analysis and Research (D-SUGAR), Japan Agency for Marine-Earth Science and Technology, Yokosuka, Kanagawa 237-0061, Japan
[g] Graduate School of Environment and Information Sciences, Yokohama National University, 79-7 Tokiwadai, Hodogaya-ku, Yokohama 240-8501, Japan
[h] Ore Genesis Research Unit, Project Team for Development of New-generation Research Protocol for Submarine Resources, Japan Agency for Marine-Earth Science and Technology, Yokosuka, Kanagawa 237-0061, Japan
[i] Center for Socio-Robotic Synthesis, Kyushu Institute of Technology, 2-4 Hibikino, Wakamatsu-ku, Kitakyuushu 808-0196, Japan

ARTICLE INFO

Article history:
Received 1 April 2016
Received in revised form
15 August 2016
Accepted 27 August 2016
Available online 28 August 2016

Keywords:
Vent-ecology
Ecological mapping
Visual survey
3D reconstruction
Underwater vehicle

ABSTRACT

This paper describes a method to survey the distribution of megabenthos over multi-hectare regions of the seafloor. Quantitative biomass estimates are made by combining high-resolution 3D image reconstructions, used to model spatial relationships between representative taxa, with lower-resolution reconstructions taken over a wider area in which the distribution of larger predatory animals can be observed. The method is applied to a region of the Iheya North field that was the target of scientific drilling during the IODP Expedition 331 in 2010. An area of 2.5 ha was surveyed 3 years and 4 months after the site was drilled. More than 100,000 organisms from 6 taxa were identified. The visible effects of drilling on the distribution of megabenthos were confined to a 20 m radius of the artificially created hydrothermal discharges, with the associated densities of biomass lower than observed in nearby naturally discharging areas.

1. Introduction

Deep-sea hydrothermal systems can support diverse and densely populated biological communities (Corliss et al., 1979; Spiess et al., 1980; Rona et al., 1986). While primary production in surface communities is typically based on photosynthesis, deep-sea vent ecosystems largely rely on the metabolic activity of free-living and symbiotic microorganisms that form the basis of chemosynthetic communities. The primary production of these microorganisms and the diverse communities of megabenthos they support rely on the oxidisation of reduced inorganic compounds in discharging hydrothermal fluids (Jannasch et al., 1989; Wirsen et al., 1993; Bach and Edwards, 2003; Cowen et al., 2003; Bachraty et al., 2009). As a result, any changes in seafloor hydrothermal fluid discharge can have an impact on the distribution and abundance of these communities (Juniper et al., 1992; Shank et al., 1998; Copley et al., 1999; Kawagucci et al., 2013; Nakajima et al., 2015). The interest in deep-sea mining raises concern about the potential impacts of human activities in these areas and drives the need to develop ways to systematically assess the response of these complex ecosystems over wide-areas (Glover and Smith, 2003; Gena, 2013; Van Dover, 2014).

The distribution of microbial and megabenthic biomass on the seafloor has been the subject of several studies over the past decades and many of the functional relationships that drive these ecosystems have been clarified (Jannasch and Mottl, 1985; Fisher et al., 1994; Johnson et al., 1994; McCollom and Shock, 1997; Sarrazin et al., 1999; Desbruyères et al., 2000; Luther et al., 2001; Van Dover et al., 2002; Bergquist et al., 2007; Nakamura and Takai, 2014). However, while primary production is strongly related to

* Corresponding author at: Southampton Marine and Maritime Institute, University of Southampton, Southampton SO16 7QF, UK.
E-mail address: B.Thornton@soton.ac.uk (B. Thornton).
[1] Current address: Scripps Institution of Oceanography, University of California San Diego, 9500 Gilman Drive, La Jolla, CA 92083-0202, USA.

http://dx.doi.org/10.1016/j.dsr.2016.08.009

the physical and chemical characteristics of discharging hydrothermal fluids (Bach and Edwards, 2003; Nakamura and Takai, 2015), chemical and temperature gradients in these areas can be steep and can change rapidly in time. Furthermore, the interactions between different taxa of animals are complex, making it difficult to apply these relationships to make bounded predictions of biomass. At the same time, direct observation of megabenthic animals, which typically range from centimetres to tens of centimetres in size, generally requires color images to be taken from a range of ~2 m to achieve sufficient contrast and spatial resolution to identify individuals (ind.) from different taxa (Connelly et al., 2012; Nakajima et al., 2015). While these images can be combined into 2D mosaics (Palterson, 1975; Marks et al., 1995; Pizarro and Singh, 2003) or 3D image reconstructions (Negahdaripour and Madjidi, 2003; Nicosevici et al., 2009; Pizarro et al., 2009; Johnson-Roberson et al., 2010; Bodenmann et al., 2010, 2016), the limited footprint of each image combined with the difficulty of accessing these remote environments has confined visual surveys of megabenthos in hydrothermally active seafloors to spatial scales of 100–1,000 m^2 (Podowski et al., 2009, 2010; Kim and Hammerstrom, 2012; Marsh et al., 2012, 2013; Sen et al., 2013, 2014). Visual surveys over multi-hectare regions have been demonstrated by obtaining seafloor imagery from higher altitudes of ~8 m (Escartin et al., 2008; Bodenmann et al., 2013; Kwasnitschka et al., 2016). However, the increased coverage comes at the cost of resolution and detailed survey of seafloor biota distribution over these spatial scales has not yet been realised. Since it is not uncommon for hydrothermal fields to extend over several hectares (Hannington et al., 1995, 2011; Tsuji et al., 2012), the technical limitation in our ability to observe these areas at sufficient resolution over the necessary spatial scales means that the distribution and abundance of vent-endemic biological communities over entire vent-fields remains uncertain.

In this work, the authors apply the concept of using surrogate taxa (Kremen, 1992; Wiens et al., 2008) to estimate the quantitative distribution of vent-endemic megabenthic biological communities over multiple hectares of seafloor. The method uses underwater robots equipped with instruments to generate multi-resolution 3D image reconstructions of the seafloor that can efficiently observe deep-sea benthic environments on spatial scales that cannot otherwise be practically achieved. The method is applied to survey the distribution of vent-endemic megabenthic communities in a multi-hectare region of the Iheya North field located in the Okinawa Trough (27°45.50′N 126°53.90′E, Fig. 1). The site is a hydrothermal field at a depth of ~1,000 m that was drilled during the Integrated Ocean Drilling Program (IODP) Expedition 331 in September 2010 (Takai et al., 2011, 2012). The site is characterised by a thick layer of sediments and the presence of several large chimneys (Tsuji et al., 2012), with the 20 m high North Big Chimney (NBC) mound at the centre of its activity (Fig. 1 (d)). While 33 species of fauna have been reported to exist in the Iheya North Field (Nakajima et al., 2014; Watanabe et al., 2015) the majority of megabenthic biomass is composed of 3 chemosynthetic taxa, the *Shinkaia crosnieri* galatheid crab and two species of *Bathymodiolus* mussel, where genetic studies have shown that the *B. platifrons* and *B. japonicus* are the only species of *Bathymodiolus* in the Iheya North field (Fujiwara et al., 2000). In addition to these main taxa, alvinocaridid shrimps have also been reported to form

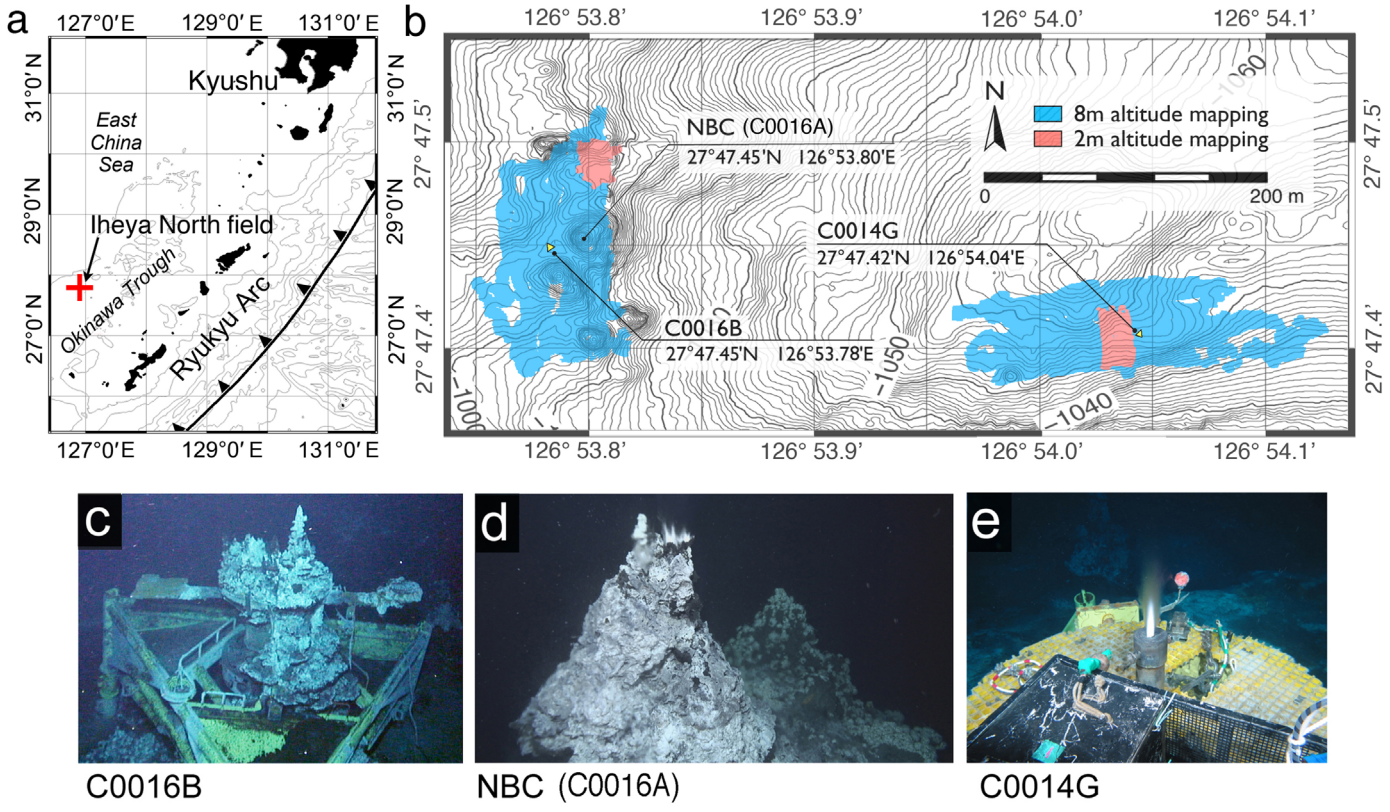

Fig. 1. Location of the Iheya North field in the East China Sea. (a) Regional location of the Iheya North field. The depth contours shown have an interval of 1,000 m. (b) Multibeam bathymetry of the surveyed area obtained using the autonomous underwater vehicle Urashima. The depth contours have an interval of 1 m. The shaded areas show regions where visual surveys were performed in this work. (c) Underwater images showing the C0016B hole and its guide base, located at the base of the NBC mound. Each edge of the triangular guide base has a length of 5.13 m. (d) Location of the C0016A hole that was drilled on top of the NBC mound. The base of the visible part of the chimney protruding from the mound has a diameter of ~5 m. (e) The C0014G hole and its guide base that was drilled in an area of sediments located ~450 m from the most active region of the Iheya North field. The diameter of the yellow circular landing platform on the guide base is 1.43 m. (For interpretation of the references to color in this figure legend, the reader is referred to the web version of this article.)

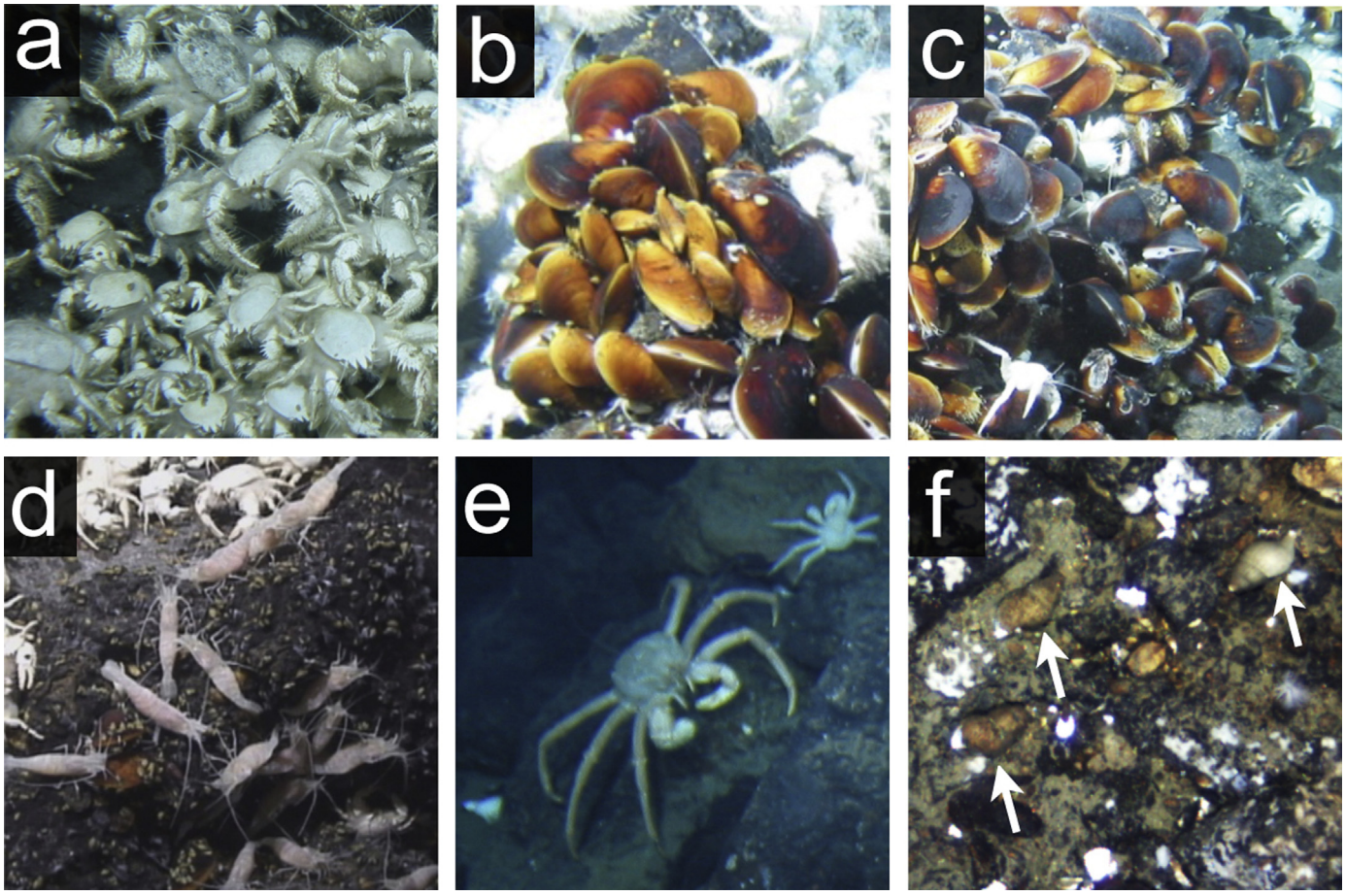

Fig. 2. Images of megabenthic vent animals representative of this region. (a) Underwater images showing an assemblage of *S. crosnieri* galatheid crab, where an average ind. measures ~4 cm along its major axis. (b) A mixed assemblage consisting predominantly of *B. platifrons* mussels, which have shells with a light orange tint. (c) A mixed assemblage consisting predominantly of *B. japonicus* mussels, which have shells that are darker in color than the *B. platifrons*. Both species of mussel measure ~5 cm along the major axis of their shells. (d) A small assemblage of alvinocaridid shrimp, each measuring ~5 cm in length. (e) Two *Paralomis* lithodid crabs, where an average ind. measures ~30 cm along its major axis. The ind. on the right of the image is located further away from the camera than the ind. on the left. (f) Three *T. desbruyeresi* (indicated by the white arrows), each of length ~8 cm along the major axis of their shell. All images shown were taken by the forward looking camera of the ROV. (For interpretation of the references to color in the text, the reader is referred to the web version of this article.)

dense assemblages in this region (Watanabe et al., 2010; Yahagi et al., 2015). While less abundant in numbers, the *Paralomis* lithodid crab and *Thermosipho desbruyeresi* whelk are the largest crustaceans and gastropods in this region, where isotopic analysis of $\delta^{15}N$ (Yamanaka et al., 2015) has shown that the *Paralomis* is a predator in the Okinawa trough and the *T. desbruyeresi* is known to be a common predator-scavenger in hydrothermal vent fields in Pacific Ocean (Sasaki et al., 2010). These 6 taxa (Fig. 2) have been cited as being representative of megabenthos in this region (Nakajima et al., 2014) and are considered in this study. In order to determine the effects of drilling on the distribution of megabenthos at this site, a two-phase seafloor imaging survey was performed in January 2014, 3 years and 4 months after the area was drilled. Two regions were surveyed during a single dive using a Remotely Operated Vehicle (ROV). The area surveyed to the west in Fig. 1(b) is centered near the NBC mound and covers the area considered the most active in the Iheya North field (Watanabe et al., 2010; Takai et al., 2011, 2012; Tsuji et al., 2012). Two holes were drilled in this region during the IODP 331 expedition. The first hole, C0016A, was drilled on top of the NBC mound and reaches a depth of 18 m below the seafloor (mbsf). The second hole, C0016B, was drilled to a depth of 45 mbsf at the base of the NBC mound. The C0016B hole is capped and an open outlet pipe is mounted on a guide base. The photo (Fig. 1(c)) shows significant growth of hydrothermal deposits around the C0016B guide base (Bodenmann et al., 2014). The other surveyed region, C0014, is located ~450 m east of the NBC mound. Assemblages of *Calyptogena okutanii* clam were identified in the central part of this region more than 10 years before it was drilled (Nakajima et al., 2015). However, pre-drilling surveys confirmed that over 90% of the *C. okutanii* were dead prior to drilling and that no endemic vent animals were present within a 15 m radius of the locations that were subsequently drilled (Takai et al., 2011, 2012; Nakajima et al., 2015). A total of 7 holes were drilled within a 10 m radius. White-colored clay-like sediments, thought to originate from drill cuttings, were observed extending 13–25 m from the centre of the drill holes during ROV surveys that took place 16 months after drilling, with the newly formed sediment layer reported to be ~300 mm thick based on the observation of buried dead *C. okutanii* clam shells on the edge of hole C0014D/E (Nakajima et al., 2015). The deepest hole, C0014G (Fig. 1(e)), was drilled to a depth of 136.7 mbsf. The inner wall of the C0014G hole is lined with a casing pipe and is capped with an open outlet pipe mounted on a guide base. The temperature of the post-drilling hydrothermal discharge of the drill-hole has been measured at 311 °C (Kawagucci et al., 2013). The photo, which was taken during the ROV dive described in this study, shows that the hole has remained active for an extended period. The penetration depths of the other holes drilled in this region range from 4.2 to 44.5 mbsf (Takai et al., 2011, 2012). Details concerning the drill-holes that were surveyed

Table 1
Details of the holes drilled during IODP 331 that were surveyed during this study. The values for temperature are as reported in Kawagucci et al., 2013. The locations of holes C0014F and C0014G have been updated from previous publications (Nakajima et al., 2015; Takai et al., 2011) based on the reconstructions generated in this study.

Region	Hole	Latitude (N)	Longitude (E)	Seafloor depth (m)	Penetration depth (mbsf)	Maximum temperature at orifice (°C)	Comments
NBC	C0016A	27°47.4548′	126°53.8034′	982.0	18.0	310	Bare hole, located on top of NBC mound
	C0016B	27°47.4538′	126°53.7860′	995.0	44.9	308	Bare hole, guide base
C0014	C0014A	27°47.4140′	126°54.0487′	1059.5	6.5	-	Bare hole
	C0014B	27°47.4131′	126°54.0448′	1059.0	44.5	-	Bare hole
	C0014C	27°47.4194′	126°54.0391′	1060.0	6.5	-	Bare hole
	C0014D	27°47.4158′	126°54.0406′	1060.0	16.0	301	Bare hole
	C0014E				35.0		
	C0014F	27°47.4185′	126°54.0443′	1060.8	4.2	-	Bare hole
	C0014G	27°47.4165′	126°54.0463′	1059.8	136.7	311	Casing pipe, guide base

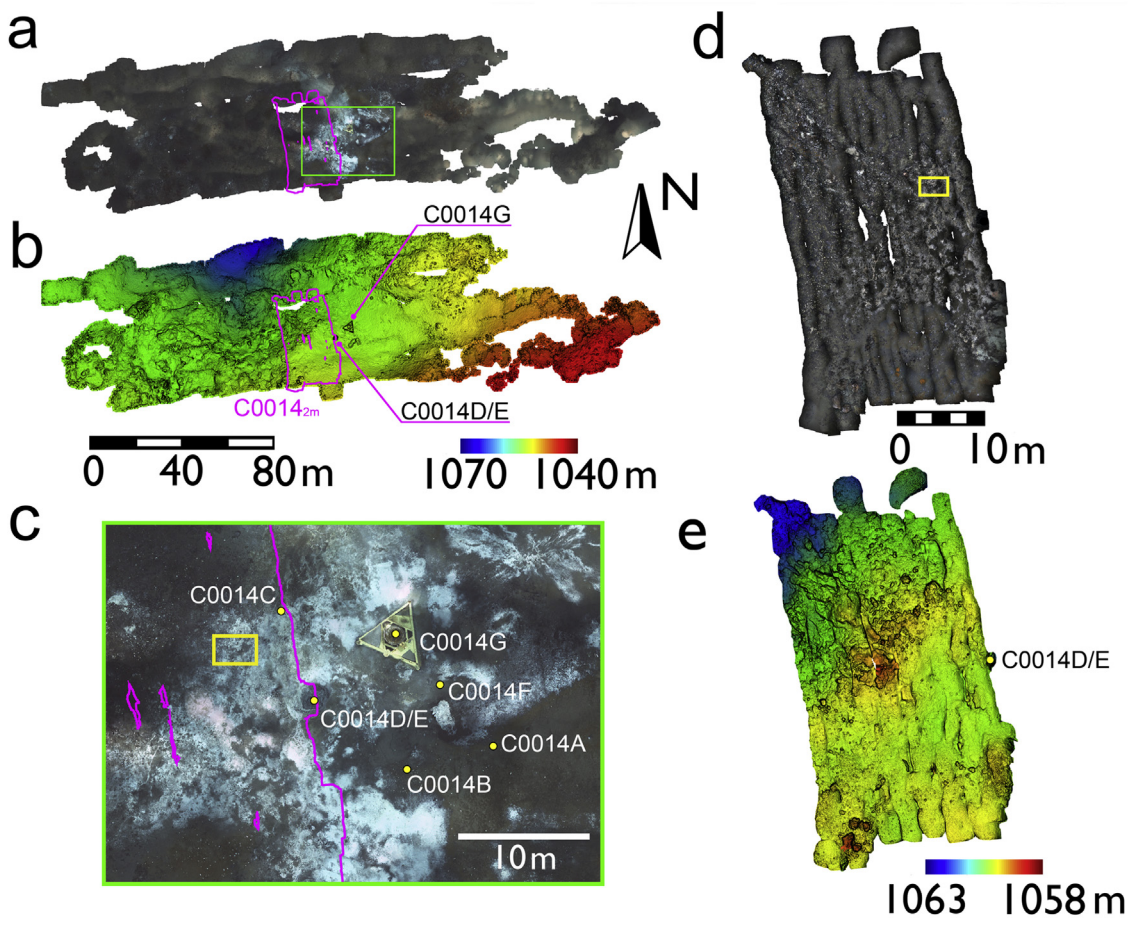

Fig. 3. Reconstruction of the C0014 region. (a) Orthographic top view projection of the wide-area reconstruction C0014$_{8m}$ that was surveyed from an altitude of ~8 m. The green outline shows the boundary of the close-up view of the drilled region in (c). The purple outline shows the boundary of the high-resolution reconstruction C0014$_{2m}$ in (d). (b) The corresponding bathymetry generated using the stereo-images, with the boundary of the high-resolution bathymetry shown by the purple outline. (c) Close-up view of the drilled region in C0014$_{8m}$ that is outlined in green in (a). (d) Orthographic top view projection of the high-resolution reconstruction C0014$_{2m}$ that was surveyed from an average altitude of ~2 m in the region outlined in purple in (a)–(c). (e) The corresponding bathymetry generated using the stereo-images. The areas outlined in yellow in (c) and (d) highlight the same area of seafloor and are shown in more detail in Fig. 5. (For interpretation of the references to color in this figure legend, the reader is referred to the web version of this article.)

during this study are summarised in Table 1. It should be noted that the locations of holes C0014F and C0014G have been updated from previous publications (Nakajima et al., 2015; Takai et al., 2011) based on the reconstructions generated in this study. High temperature venting has been confirmed at the C0016A and C0016B holes and the C0014D/E and C0014G holes (Kawagucci et al., 2013). Diffuse flows were observed seeping out of the sediments near the C0014 drill-site where the seafloor is discolored in Fig. 3(c) and also around the C0016B drill-hole. Diffuse flows were also observed seeping out of several of the mounds and rocky outcrops in the NBC region. Studies have shown that physical and chemical alterations have taken place locally within a few meters of the drill-holes (Kawagucci et al., 2013; Thornton et al., 2015), with local changes in vent communities also reported (Nakajima et al., 2015). However, the effects of the sustained hydrothermal discharge are not well understood for spatial scales larger than a few meters. The results of this work provide valuable insight regarding the impacts of anthropogenic drilling on deep-

sea vent-endemic biological communities over multi-hectare spatial scales.

2. Seafloor imaging

2.1. Method

Surveys were conducted using the ROV Hyperdolphin of the Japan Agency for Marine-Earth Science and Technology (JAMSTEC) during the KY14-01 cruise of the R/V Kaiyo. The ROV was equipped with two imaging systems and a two-phase survey was carried out to obtain seafloor imagery at different resolutions. Wide-area surveys were performed in the regions shown in blue in Fig. 1 (b) from a high-altitude of ~8 m using the SeaXerocks long-range 3D seafloor imaging instrument (Bodenmann et al., 2013). Seafloor imagery covering a total area of 2.5 ha was obtained in ~6 h from this altitude. Overlapping areas, shown in red in Fig. 1(b), were surveyed at higher resolution from an altitude of ~2 m using the Serpent 3D seafloor imaging instrument (Le Dantec et al., 2013). A total area of ~1,500 m^2 was surveyed in ~3 h from this altitude. Overlapping areas of the seafloor were surveyed consecutively and all seafloor observations were completed in ~10 h during a single ROV dive. The instruments used in this study each consist of downward-looking digital still stereo-pair cameras, where each system contains the necessary electronics to drive synchronised flashes and store the acquired images. SeaXerocks uses 4 synchronised Xenon flash lamps for illumination of the seafloor and images are acquired at an interval of 5 s. The Serpent has 2 synchronised LED flashes and images are acquired at an interval of 0.5 s. Vehicle navigation data was acquired using a 1.2 MHz Doppler velocity log (DVL: Teledyne RDI WHN1200), a 3-axis fiber-optic gyro (iXBlue PHINS), a pressure-depth sensor (Paroscientific, Inc. 8CB4000-I) and super short baseline (SSBL: SGK) acoustic positioning system. During the dive, data from the DVL, 3-axis gyro and depth sensor were recorded on SeaXerocks. The ROV was manually piloted along a predetermined path using the ViewXerocks waypoint graphical user interface (GUI), developed by the University of Tokyo, which provides real-time visual feedback regarding the planned and actual paths taken by the ROV together with its altitude and velocity. Lawn mower grid pattern surveys were performed with 3 orthogonal transects added to improve the accuracy of localisation in post processing. The terrain was followed at a fixed target altitude, where the overlap in the projected image area between adjacent track lines from the target altitude was set at 30% to provide full area coverage. However, due to the influence of strong currents it was not possible to achieve full coverage in the time available for data acquisition and some gaps exist in the reconstructions. SSBL data was recorded on a separate PC onboard the R/V, where the timestamps for all the data acquired were synchronised using a network time protocol (NTP) server. The images and navigation data were processed using a stereo pipeline that implements visual simultaneous localisation and mapping (SLAM) in order to generate self-consistent, geo-referenced 3D color image reconstructions (hereafter reconstructions) of the seafloor (Mahon et al., 2008; Johnson-Roberson et al., 2010).

The wide-area reconstructions generated in this study have an average resolution of ~8 mm per pixel in the horizontal plane and a vertical depth resolution of ~14 cm. The high-resolution reconstructions have an average resolution of ~1.6 mm per pixel in the horizontal plane and a vertical depth resolution of ~4 cm. The dimensional accuracy of the reconstructions is difficult to determine since high-resolution ground-truth data is not available for the natural underwater scenes imaged in this study. However, based on the known dimensions of the two guide bases that appear in the wide-area reconstructions, the average root-mean-square error in the horizontal and vertical directions can be estimated to be in the order of ~0.1 and ~0.3 m, respectively. The sources of error are inaccuracies in the calibration of the stereo-imaging instrument and in the localisation of the ROV. While there is no reference available on the seafloor to assess the accuracy of the high-resolution reconstructions, the dimensions of overlapping features are consistent with the wide-area reconstructions and it is reasonable to assume that the dimensional accuracy is no worse than that of wide-area data. It should be noted, that while the SLAM algorithm used in this work is capable of producing individually self-consistent reconstructions, the absolute position errors of the reconstructions are expected to be higher than the stated values for dimensional accuracy in the horizontal direction due to the inherent uncertainty of SSBL localisation. For a vehicle depth of ~1000 m, this would be expected to be in the region of ~10 m. The absolute accuracy in the vertical direction is expected to be of similar order to the stated value for dimensional accuracy, i.e. 0.3 m, since the error in the depth measurements when operating at a depth of ~1,000 m is <0.1 m for the pressure sensor used in this work (Jalving, 1999).

Top-view projections of the reconstructions, as shown in Figs. 3 (a) and (d) and 4(c) and (d) at reduced resolution, were used to generate geo-referenced digital labels for ind. animals. Labels were generated manually by an expert using the same taxonomy as used in Fig. 2, i.e. *S. crosnieri*, *B. platifrons*, *B. japonicus*, alvinocaridid, *Paralomis* and *T. desbruyeresi* which is considered to be the lowest level of taxonomy that can be reliably achieved using the data obtained in this work. While the two species of *Bathymodiolus* are morphologically similar (Hashimoto and Okutani, 1994; Sasaki et al., 2005) the *B. platifrons* is lighter in color and have an orange tint compared to the darker *B. japonicus*. Labeling was performed using qGIS (version 2.6.1), where the original images were also used as a reference in situations where the taxa were ambiguous or where there were possible artifacts in the reconstructions. While top views of the reconstructions were used in this work, the approach described can also be applied to 2D image mosaics. However, 2D approaches to image mosaicking suffer from inaccuracies due to perspective errors that occur in rough terrains when the imaged regions cannot be assumed piece-wise flat (Pizarro et al., 2009; Johnson-Roberson et al., 2010; Bodenmann et al., 2016; Garcia et al., 2011; Inglis et al., 2012). While this would not affect the inventory of biomass predicted using the method described, the assumption of piece-wise flat terrains would cause artifacts in the local distribution of animals in regions where vertical profiles smaller than the footprint of a single image exist.

Spatial analysis was performed using Matlab (R2011), where population densities were computed for each taxa using the geo-referenced digital labels. The densities were calculated using a Gaussian-weighted convolution operator with a 1σ diameter of 0.3 m. This was chosen based on the relative dimensional accuracy of the reconstructions in the horizontal plane (~0.1 m) in order to generate highest resolution maps of distribution that can be reliably achieved using the available data. The same spatial resolution was used for all taxa considered in this study for both the high-resolution and the wide-area reconstructions. The spatial analysis is performed by applying the convolution operator to every labeled ind. of each taxon. The cumulative sum of the operators of each taxon gives the population density distribution, which is determined for each of the taxa identified in this work. Although information about the local terrain is not directly used in our analysis of distribution, the availability of high-resolution bathymetry data is useful since the observed patterns can be interpreted in relation to their geological context. While stereo-imagery was used in this work, similarly high-resolution bathymetry can also be obtained using autonomous underwater vehicle

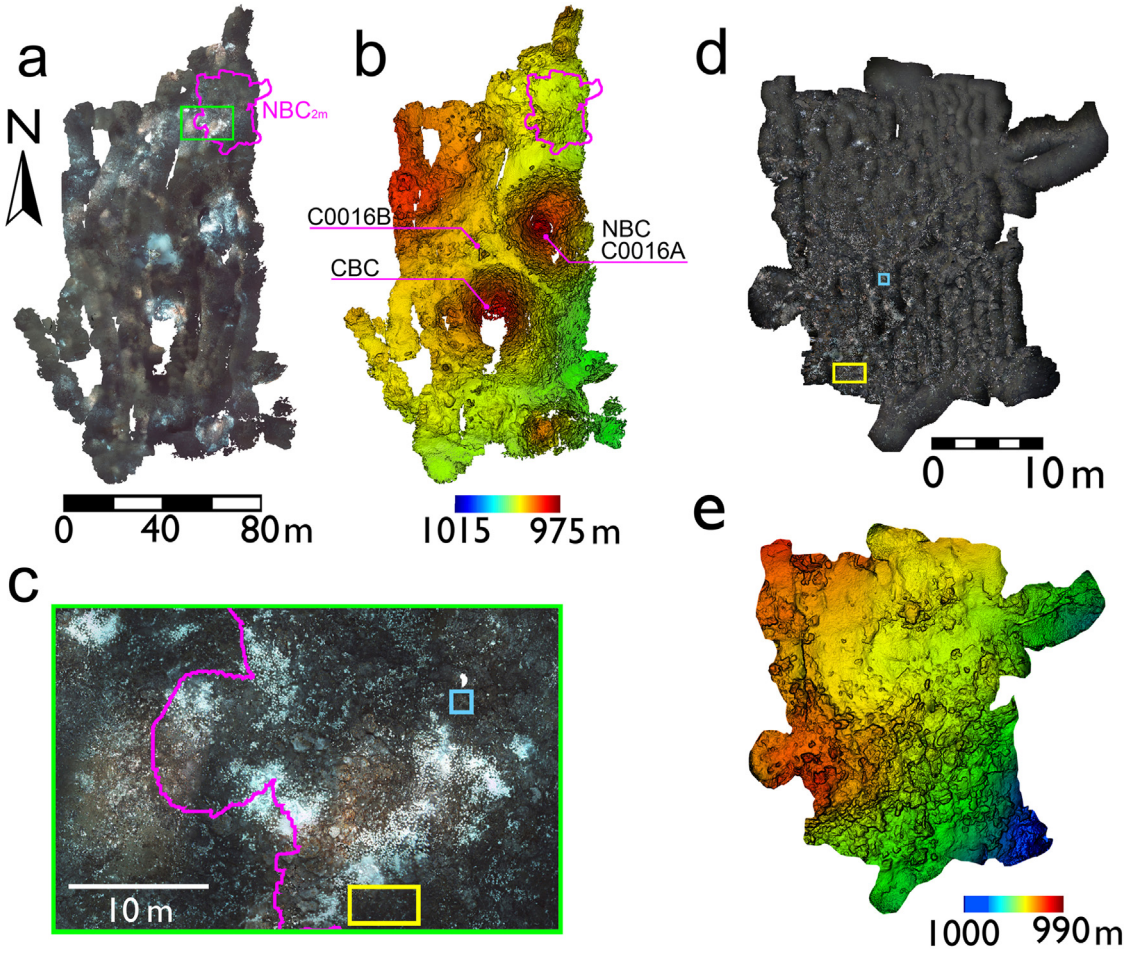

Fig. 4. Reconstruction of the NBC region. (a) Orthographic top view projection of the wide-area reconstruction NBC_{8m} surveyed from an altitude of ~8 m. The green outline shows the boundary of the close-up view of the region shown in (c). The purple outline shows the boundary of the high-resolution reconstruction NBC_{2m} in (d). (b) The corresponding bathymetry generated using the stereo-images, with the boundary of the high-resolution bathymetry shown by the purple outline. (c) Close-up view of region in NBC_{8m} that is outlined in green in (a). (d) Orthographic top view projection of the high-resolution map NBC_{2m} that was mapped from an average altitude of ~2 m in the region outlined in purple in (a)–(c). (e) The corresponding bathymetry generated using the stereo-images. The areas outlined in yellow and blue in (c) and (d) highlight the same areas of the seafloor and are shown in more detail in Fig. 5. (For interpretation of the references to color in this figure legend, the reader is referred to the web version of this article.)

(AUV) or ROV multi-beam at close range, or through the use of optical methods such light-sectioning (Bodenmann et al., 2010, 2016; Inglis et al., 2012; Massot-Campos et al., 2015), structure from motion (Garcia et al., 2011), plenoptic imaging (Dansereau and Williams, 2011) and laser time of flight (Moore and Jaffe, 2002).

2.2. Results

Fig. 3 shows top-view reconstructions and bathymetries generated near the C0014 drill-site. The wide-area reconstruction, $C0014G_{8m}$, was generated from images obtained from an average altitude of 8.4 m and covers 1.3 ha of seafloor at an average resolution of 7.9 mm (Fig. 3(a) and (b)). The green box outlines the area that was intensively drilled during the IODP 331 expedition (Nakajima et al., 2015; Takai et al., 2011, 2012). The bathymetry in Fig. 3(b) shows that the region is relatively flat with a depression towards the central north area of the surveyed region that reaches a depth of 1066 m and a shallow slope of $< 10°$ that rises towards the east of the region upto a depth of 1040 m. The drill-site is centered on a flat sediment-covered plateau of diameter ~80 m at a depth of ~1060 m. This drill-site is shown in more detail together with the locations of the drill-holes (Table 1) in Fig. 3(c). The C0014G guide base is the yellow triangular construction visible near the centre of the image with the C0014D/E drill-hole visible ~8 m southwest of it. This area was almost exclusively covered by dark sediments prior to drilling (Nakajima et al., 2015) and has been visibly altered by the post-drilling hydrothermal discharge with white discoloration of the area surrounding the drill-holes caused by both the formation of bacteria mats and mineralisation of the seafloor (Kawagucci et al., 2013). Part of the discoloration can also be attributed to drill cuttings that have settled near the drill-site (Nakajima et al., 2015). The purple outline (Fig. 3(a)–(c)) shows the $C0014_{2m}$ region where high-resolution imagery was obtained from an average altitude of 2.2 m. $C0014_{2m}$ covers an area of 846 m^2 at an average resolution of 1.5 mm (Fig. 3(d) and (e)). The C0014D/E drill-hole is located on the eastern edge of the $C0014_{2m}$. The region is relatively flat (Fig. 3(e)), with sediments covering the southeast area of the reconstruction and rocky outcrops towards the northwest. The yellow boxes in Fig. 3(c) and (d) outline the same overlapping area of seafloor in the two reconstructions. A comparison of these areas can be found in Fig. 5(a) and (b).

The wide-area reconstruction of the NBC region, NBC_{8m}, covers an area of 1.2 ha and includes the NBC mound where the C0016A hole was drilled, the C0016B guide base and several other active mounds that have not been drilled (Fig. 4(a) and (b)). Seafloor imaging was performed from an average altitude of 9 m to achieve

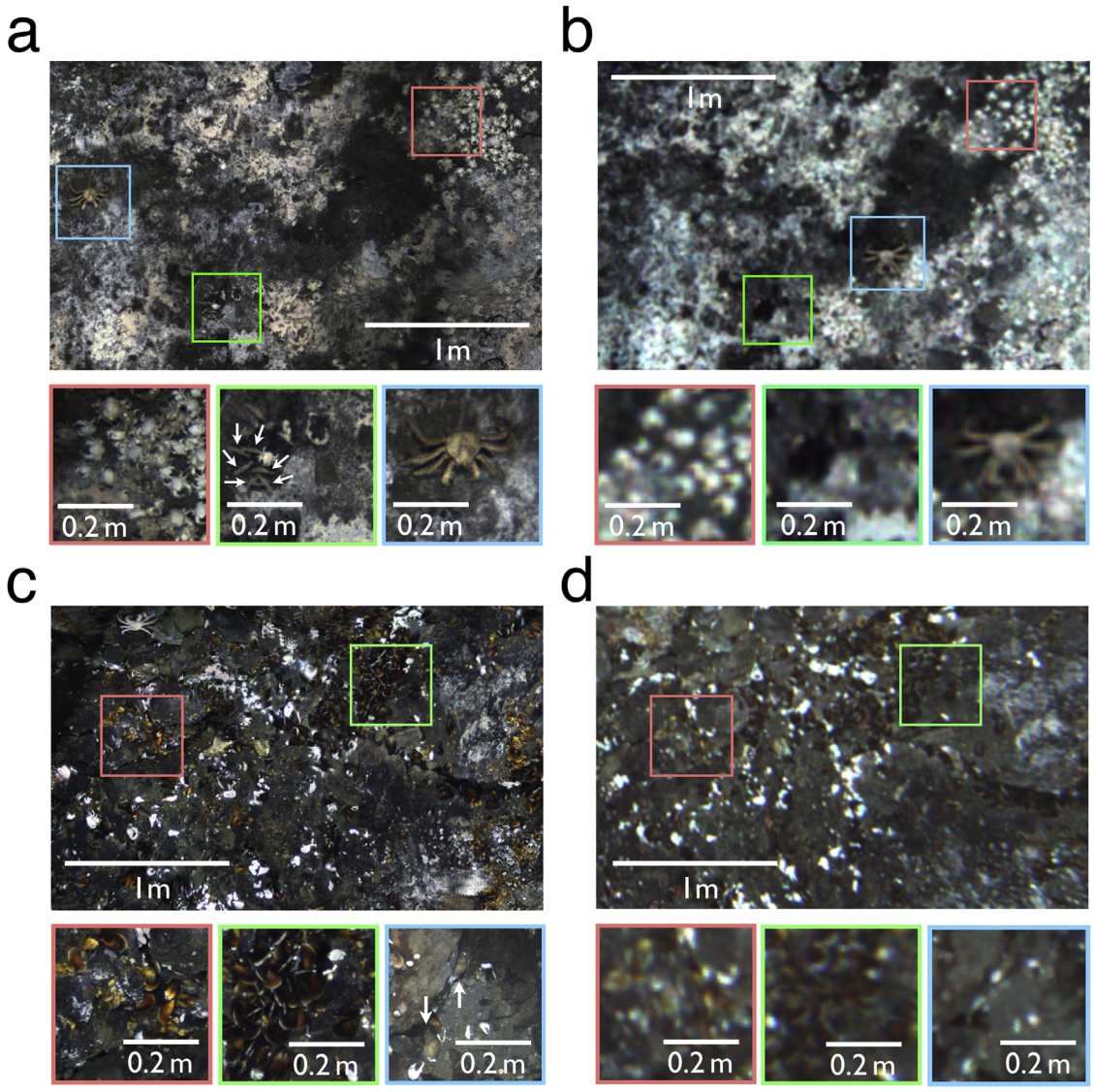

Fig. 5. Comparison of reconstructions obtained from the 2 different altitudes. The reconstructions taken from 2 m and 8 m altitude have average resolutions of 1.6 and 8.0 mm/pixel, respectively. (a) The top panel shows the yellow outlined region of $C0014_{2m}$ in Fig. 3(d) taken from ~2 m altitude. The insets show *S. crosnieri* (left), alvinocaridid (centre, indicated by white arrows) and *Paralomis* (right) observed from this altitude. (b) The top panel shows the yellow outlined region of $C0014_{8m}$ in Fig. 3(c), taken from ~8 m altitude that shows the same area of seafloor as (a), where the insets show the regions (or animal taxon in the case of the *Paralomis*) that correspond to those in (a). (c) The top panel shows the yellow outlined region of NBC_{2m} in Fig. 4(d) taken from ~2 m altitude. The insets show *B. platifrons* (left), *B. japonicus* (centre) and *T. desbruyeresi* (right, indicated by white arrows) observed from this altitude, where the region showing the *T. desbruyeresi* is located in the blue outlined region of NBC_{2m} in Fig. 4(d). (d) The top panel shows the yellow outlined region of NBC_{8m} in Fig. 4(c) taken from ~8 m altitude that shows the same area of seafloor as (c), where the insets correspond to those in (c). The location of the bottom right panel in (d) is indicated by the blue outlined region of NBC_{8m} in Fig. 4(c). (For interpretation of the references to color in the text, the reader is referred to the web version of this article.)

Table 2
Individuals identified in the $C0014_{2m}$, NBC_{2m}, $C0014_{8m}$ and NBC_{8m} regions together with the average and maximum population densities of each species. The location of each region is shown in Fig. 1 and the individual reconstructions are shown in Figs. 3 and 4. The projected planar areas of the high-resolution reconstructions $C0014_{2m}$ and NBC_{2m} are 846 and 695 m^2 with average pixel resolutions of 1.5 and 1.8 mm, respectively. The projected planar areas of the wide-area reconstructions $C0014_{8m}$ and NBC_{8m} are 1.3 and 1.2 ha with average resolutions of 7.9 and 8.2 mm, respectively. While all 6 taxa in Fig. 2 were identified in the high-resolution reconstructions, only the *S. crosnieri* and *Paralomis* could be reliably identified in the wide-area reconstructions. The values of σ_{2m} represent the densities above which 68.2% of the ind. of each taxa are found in the high-resolution reconstructions.

Species	$C0014G_{2m}$			NBC_{2m}			σ_{2m} ind./m^2	$C0014G_{8m}$			NBC_{8m}		
	Ind.	Density ind./m^2		ind.	density ind./m^2			ind.	density ind./m^2		ind.	density ind./m^2	
		Av.	Max.		Av.	Max.			Av.	Max.		Av.	Max.
S. crosnieri	3,536	4.2	319	7,160	10	465	54	6,336	0.50	274	47,335	3.9	393
B. platifron	7,282	8.6	863	12,885	19	597	99	–	–	–	–	–	–
B. japonicus	6,780	8.0	498	7,339	11	494	99	–	–	–	–	–	–
Alvinocaridid	170	0.20	170	500	0.72	186	16	–	–	–	–	–	–
Paralomis	96	0.11	29	109	0.16	18	2.8	195	0.015	11	1,050	0.086	16
T. desbruyeresi	12	0.014	19	7	0.010	19	3.8	–	–	–	–	–	–
Total ind.	17,876	–	–	28,000	–	–	–	6,531	–	–	48,385	–	–

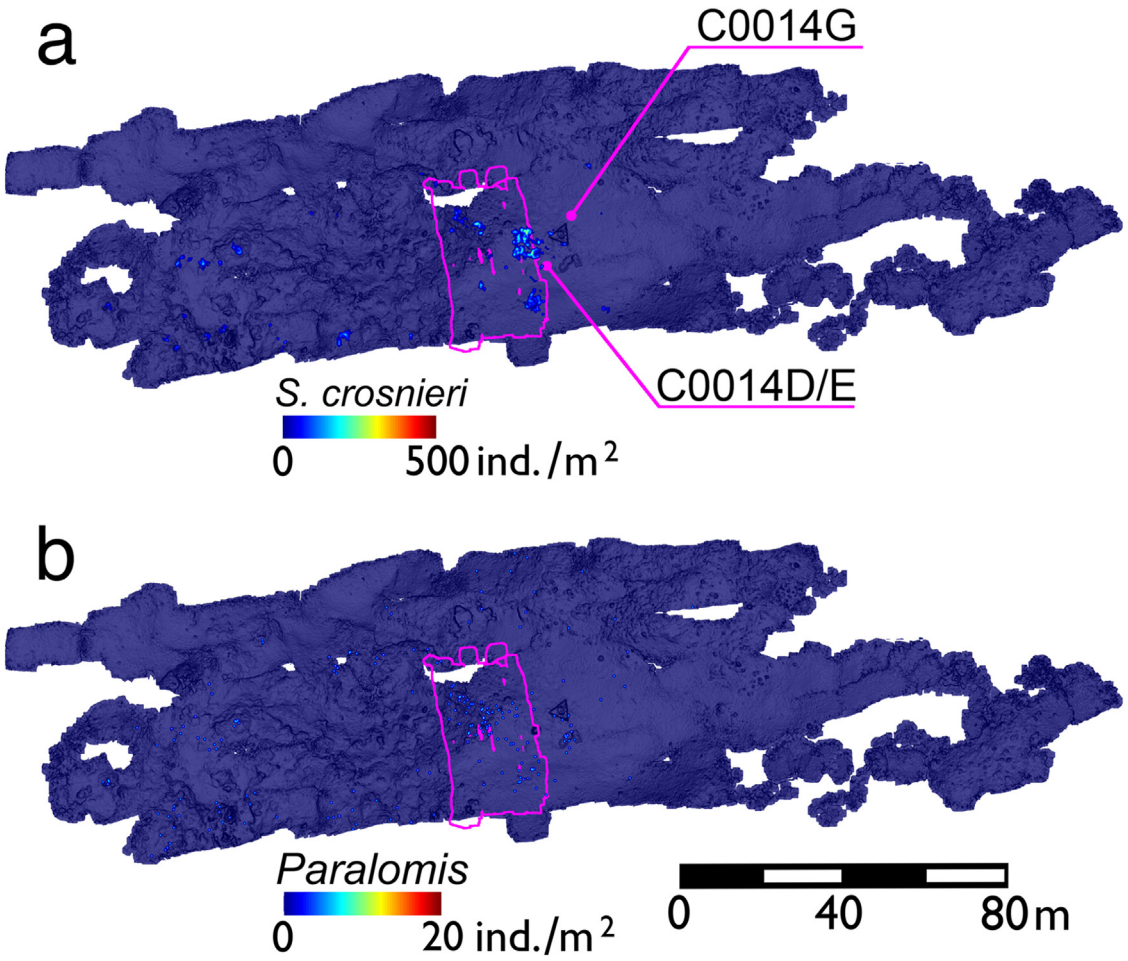

Fig. 6. Population density maps for the $C0014_{8m}$ region. (a) The density distributions of *S. crosnieri*, and (b) *Paralomis* identified in the reconstruction. The *S. crosnieri* form densely packed assemblages and are most abundant near the drill-site. While the *Paralomis* do not form assemblages they also tend to be located near the drill-site. (For interpretation of the references to color in the text, the reader is referred to the web version of this article.)

an average resolution of 8.2 mm. The region is characterised by extremely rough, rocky terrains with steep slopes and strong vertical profiles of several tens of meters, as seen in Fig. 4(b). The NBC and CBC mounds each have a diameter of ~40 m and measure ~20 m in height. In addition to these large mounds, there exist several smaller mounds and rocky outcrops in the surveyed area, where most of these have active diffuse flows. The C0016B guide-base is located at the base of the NBC and CBC mounds in an area that is relatively flat and is covered by sediments. The area outlined in green, shown in more detail in Fig. 4(c), is a natural hotspot for bioactivity located 40 m north of the NBC mound. The high-resolution reconstruction NBC_{2m} in Fig. 4(d) and (e) fills the area outlined in purple in Fig. 4(a)–(c), and shows this area in more detail. Here seafloor imaging was performed from an average altitude of 2.6 m to cover 695 m^2 of the seafloor at an average resolution of 1.8 mm. The bathymetry in Fig. 4(e) shows that the southern part of this region is sloped by ~25° downwards to the east, with exposed rocky outcrops at a depth of 990 m towards the west of the reconstruction. The northern part of the high-resolution reconstruction is less steeply sloped (~10°) and is covered by sediments. The yellow and blue boxes in Fig. 4(c) and (d) highlight the same area of seafloor in the two reconstructions. A comparison of these highlighted areas can be found in Fig. 5(c) and (d).

A total of 100,792 ind. from 6 different taxa were identified in the reconstructions and digital labels were generated. A summary of the animals identified in each reconstruction is given in Table 2. While ind. from all 6 of the taxa in Fig. 2 can be identified in the high-resolution reconstructions ($C0014_{2m}$ and NBC_{2m}), the resolution and color contrast in the wide-area reconstructions ($C0014_{8m}$ and NBC_{8m}) is only sufficient for reliable detection of *S. crosnieri* and *Paralomis*. The results of the spatial analyses in the $C0014_{8m}$, $C0014_{2m}$, NBC_{8m} and NBC_{2m} regions are shown in Figs. 6–9, respectively. Fig. 10 shows histograms of the number of ind. of each taxon identified at a particular population density in the high-resolution reconstructions (Figs. 7 and 9). The red lines represent the population densities above which $>68.2\%$ of the total number of ind. of each taxon are found in the high-resolution data, where the numerical values, σ_{2m}, determined from the data are given in Table 2. The delineated maps in Figs. 11(a) and (b) and 12(a) and (b) show the areas where the population density of each taxon is larger than the corresponding value of σ_{2m}. These are overlaid onto grey-scale shaded relief maps generated from the seafloor bathymetry. Figs. 11(c) and 12(c) show the relative populations of each of the taxa identified in the high-resolution data.

Three chemosynthetic species *S. crosniori*, *B. platifrons* and *B. japonicus* form assemblages with maximum densities of >400 ind./m^2. These taxa are found in areas where diffuse hydrothermal fluids are visibly discharged from the seafloor. The two species of *Bathymodiolus* mussel are found in mixed assemblages that can cover areas of several meters in diameter (Figs. 7(b) and (c),11 (b) and 9(b) and (c) and 12(b)). *B. japonicus* are typically surrounded by *B. platifrons*, possibly indicating a niche separation for certain physical and chemical conditions (Fujiwara et al., 2000; Kyuno et al., 2009). Both species of mussel attach themselves to

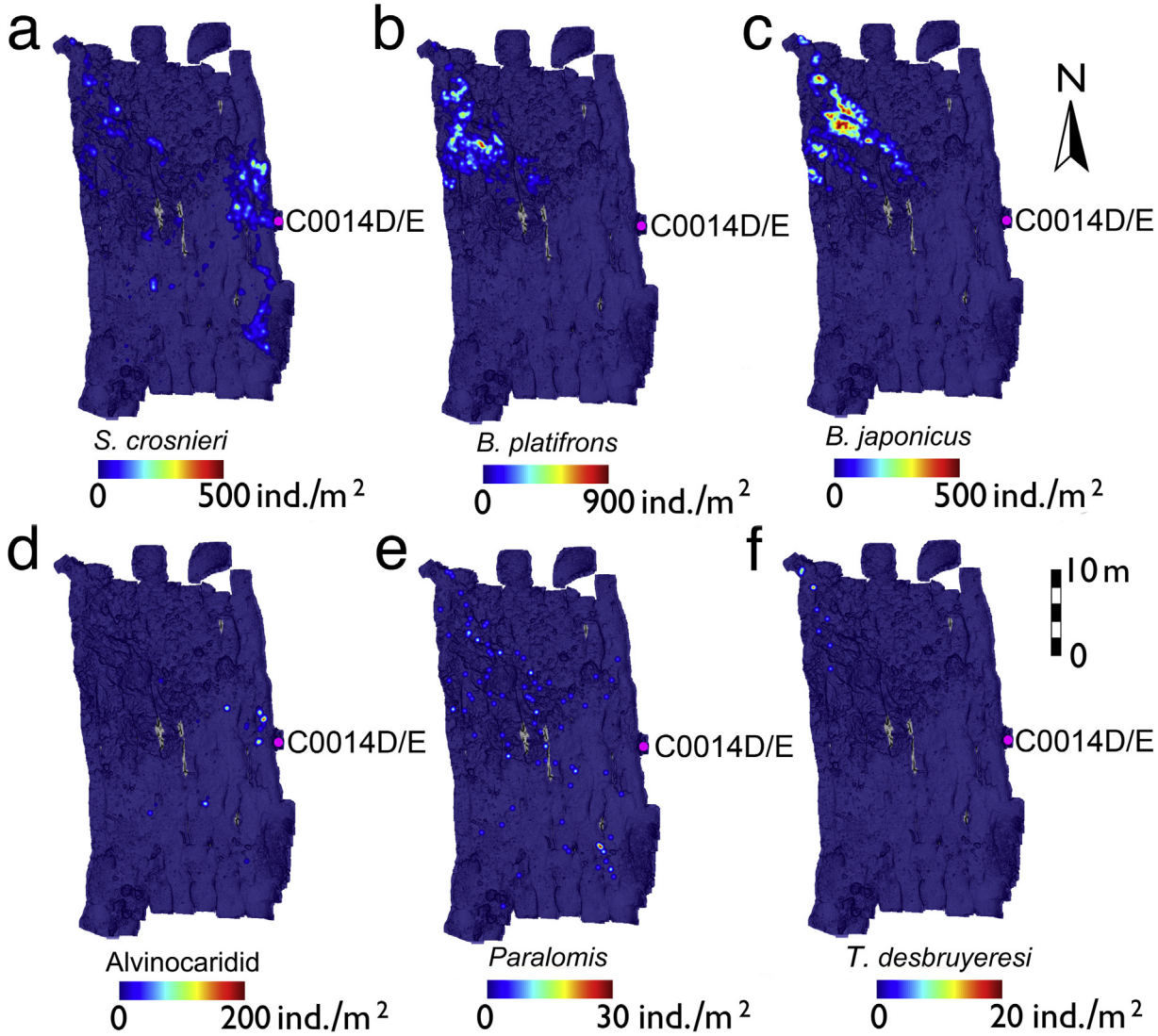

Fig. 7. Population density maps for the $C0014_{2m}$ region. (a) The *S. crosnieri* form dense assemblages, where the highest population density is found on the eastern side of the region in sediment covered areas with active diffuse flows. Both the (b) *B. platifrons* and (c) *B. japonicus* form dense assemblages located in the rocky outcrop at the northwest of the reconstruction. (d) The Alvinocaridid shrimp form smaller assemblages than the *S. crosnieri* and *Bathymodiolus* mussels and are located in the sediment covered region on the eastern side of the reconstruction in areas with diffuse flows. (e) The *Paralomis* are dispersed in areas that are covered by sediments and have exposed rocky outcrops, with a tendency to be located near dense *S. crosnieri* and *Bathymodiolus* assemblages. (f) The *T. desbruyeresi*, do not form assemblages and are found on the rocky outcrop at the northwest of the reconstruction near assemblages of *S. crosnieri* and *Bathymodiolus* mussels. (For interpretation of the references to color in the text, the reader is referred to the web version of this article.)

exposed rocks and the influence of the type of seafloor on their distribution can be clearly seen in the data. While no ind. from these species are observed in sediment-covered areas, dense assemblages are found on rocky outcrops that are both flat (e.g. northwest of $C0014_{2m}$) and steeply sloped (e.g. southwest of NBC_{2m} with a slope of $\sim 25°$).

S. crosnieri are also found in similar areas to the *Bathymodiolus* mussel. However, while *Bathymodiolus* mussels are observed on steeply sloped surfaces, assemblages of are typically found on surfaces that are sloped by $< 10°$, as can be seen in the NBC_{8m} and NBC_{2m} regions in Figs. 4(b),8(a) and 4(e) and 9(a) where assemblages are not observed on the slopes of the NBC and CBC mounds. This is also noticeable in the southwest part of the NBC_{2m} region, where the assemblages of *S. crosnieri* are located on a small ledge at the top of a steep slope, and not on the slope itself. Their distribution however, is not limited to exposed rock surfaces. Dense assemblages of *S. crosnieri* are found in the hydrothermally altered region of site C0014 that was intensively drilled (Figs. 6(a), 7 (a) and 11(a) and (b)) and at the base of the C0016B guide (Figs. 8 (a) and 12(a)). In each case the relief is smooth in these areas since the seafloor covered by sediments. The remaining 3 taxa account for $< 3\%$ of the ind. identified in the high-resolution reconstructions. The alvinocaridid form small assemblages of diameter < 0.3 m with maximum densities of > 180 ind./m^2. These are located near assemblages of *S. crosnieri* and are found in both rocky and sediment-covered areas. The *Paralomis* is a predator that potentially lies at the top of the food-chain in the Iheya North field. Individuals of this taxon measure ~ 0.3 m along their major axis and comprise between 0.4–0.5% of the total number of ind. observed in the high-resolution reconstructions. While the *Paralomis* are sparsely distributed, they have a tendency to be found near dense assemblages of other animals. This is seen in the high-resolution reconstruction NBC_{2m} (Fig. 12(b)) where the *Paralomis* are found near mixed assemblages of chemosynthetic species on the rocky outcrop. *Paralomis* are also found near assemblages that consist of only *S. crosnieri* in sediment-covered areas, such as the east of $C0014_{2m}$ (Fig. 11(b)) and near assemblages that consist mainly of *Bathymodiolus* mussel in the rocky outcrop to the west of

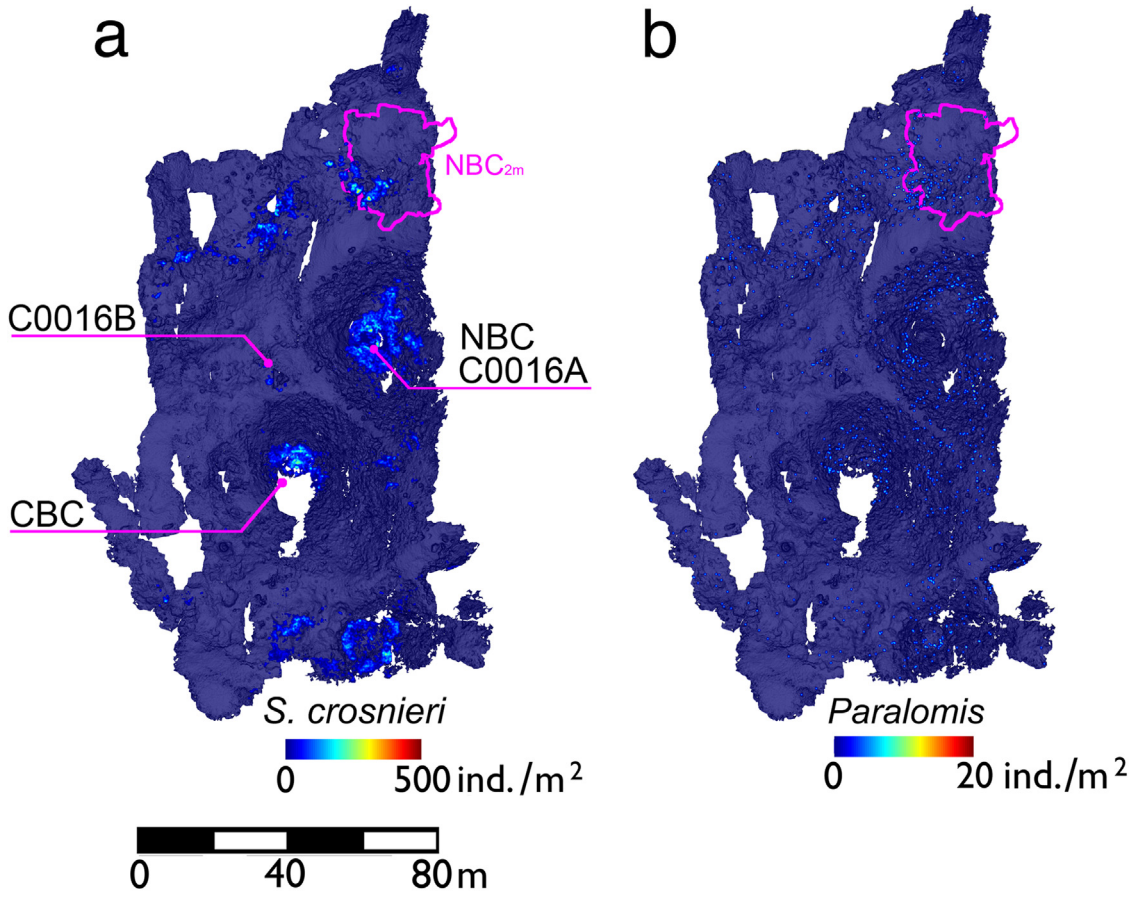

Fig. 8. Population density maps for the NBC_{8m} region. (a) The density distributions of *S. crosnieri*, and (b) *Paralomis* identified in the reconstruction. The *S. crosnieri* form large assemblages on mounds and rocky outcrops. While the *Paralomis* do not form assemblages, it is clear from the distribution that the *Paralomis* also tend to be located near areas where there are assemblages of *S. crosnieri*. (For interpretation of the references to color in the text, the reader is referred to the web version of this article.)

$C0014_{2m}$. This pattern is also seen in the wide-area reconstructions (Figs. 11(a) and 12(a)), where the *Paralomis* tend to be located near assemblages of *S. crosnieri*, which is the only chemosynthetic taxon identified at the lower-resolution. *Paralomis* are also observed on steep surfaces such as on the slopes of the NBC and CBC mounds, which are sloped by $>30°$. The distribution patterns observed suggest that the *Paralomis* are not confined to any particular type of terrain and do not have any obvious preference to be located near a specific type of prey. The *T. desbruyeresi* also tend to be distributed amongst the chemosynthetic animals, though the number of ind. identified in this work is too few to draw any further insight.

The densities of *Bathymodiolus* mussel observed in the $C0014_{2m}$ and NBC_{2m} regions are similar in order to those reported by Fujikura et al. (2002) for a 546 m^2 region of the Minami-Ensei Knoll, a hydrothermally active site located 100 km north of the Iheya North field at a depth of between 600–740 m. The average density of *Bathymodiolus* in the Knoll was reported to be 53.0 ind./m^2 with a maximum density 644 ind./m^2. The average density of *Bathymodiolus* (combined *B. japonicus* and *B. platifrons*) for the $C0014_{2m}$ and NBC_{2m} regions determined in this work are 16.6 and 29.1 ind./m^2 with maximum densities of 863 and 597 ind./m^2, respectively. While the maximum density of *Paralomis* sp. in the Knoll is not reported, the average density of 0.4 ind./m^2 is in the same order as in the $C0014_{2m}$ (av. 0.11 ind./m^2) and NBC_{2m} (av. 0.16 ind./m^2) regions. Similar densities have also been reported in the Lau Basin by Podowski et al. (2010), where the average density of *Paralomis* sp. observed in a 195 m^2 region was 0.11 ind./m^2. While density of *Bathymodiolus* sp. in the Lau Basin is not reported, the average density of *T. desbruyeresi* (1.0 ind./m^2) is significantly higher than in the $C0014_{2m}$ (0.014 ind./m^2) and NBC_{2m} (0.010 ind./m^2) regions. The population densities for alvinocaridid in the $C0014_{2m}$ (0.20 ind./m^2) and NBC_{2m} (0.72 ind./m^2) regions are of similar order to the Lau Basin (1.2 ind./m^2), but are lower than in the Minami-Ensei Knoll (3.2 ind./m^2). While the maximum densities of alvinocaridid in the Minami-Ensei Knoll and Lau Basin are not reported, the maximum values in the $C0014_{2m}$ (170 ind./m^2) and NBC_{2m} (186 ind./m^2) regions are an order of magnitude lower than the densities of $>2{,}000$ ind./m^2 estimated at the Von Damm Vent field (2,300 m depth) and the Beebe Vent field (4960 m depth) located in the Mid-Cayman spreading centre (Connelly et al., 2012). The values of density should however be treated with caution when making inter-site comparisons since the distribution of megabenthos in hydrothermally active areas have high local variability and the observational footprints of visual surveys are small, typically in the order of a few hundred m^2. This point is illustrated by the observations made in this study, where the average population densities of the *Paralomis* and *S. crosnieri* in the wide-area reconstructions $C0014_{8m}$ and NBC_{8m} are between 12% and 55% of the respective average densities observed in the smaller $C0014_{2m}$ and NBC_{2m} sub-regions.

The main sources of uncertainty in determining the distribution of megabenthos in this study lie in the labeling of the georeferenced reconstructions. The dimensional accuracy of the reconstructions is $\sim$0.1 m in the horizontal plane, which is smaller than the resolution of the convolution window used to determine population density, and the use of a 3D approach to generate the image reconstructions means that the distributions determined do

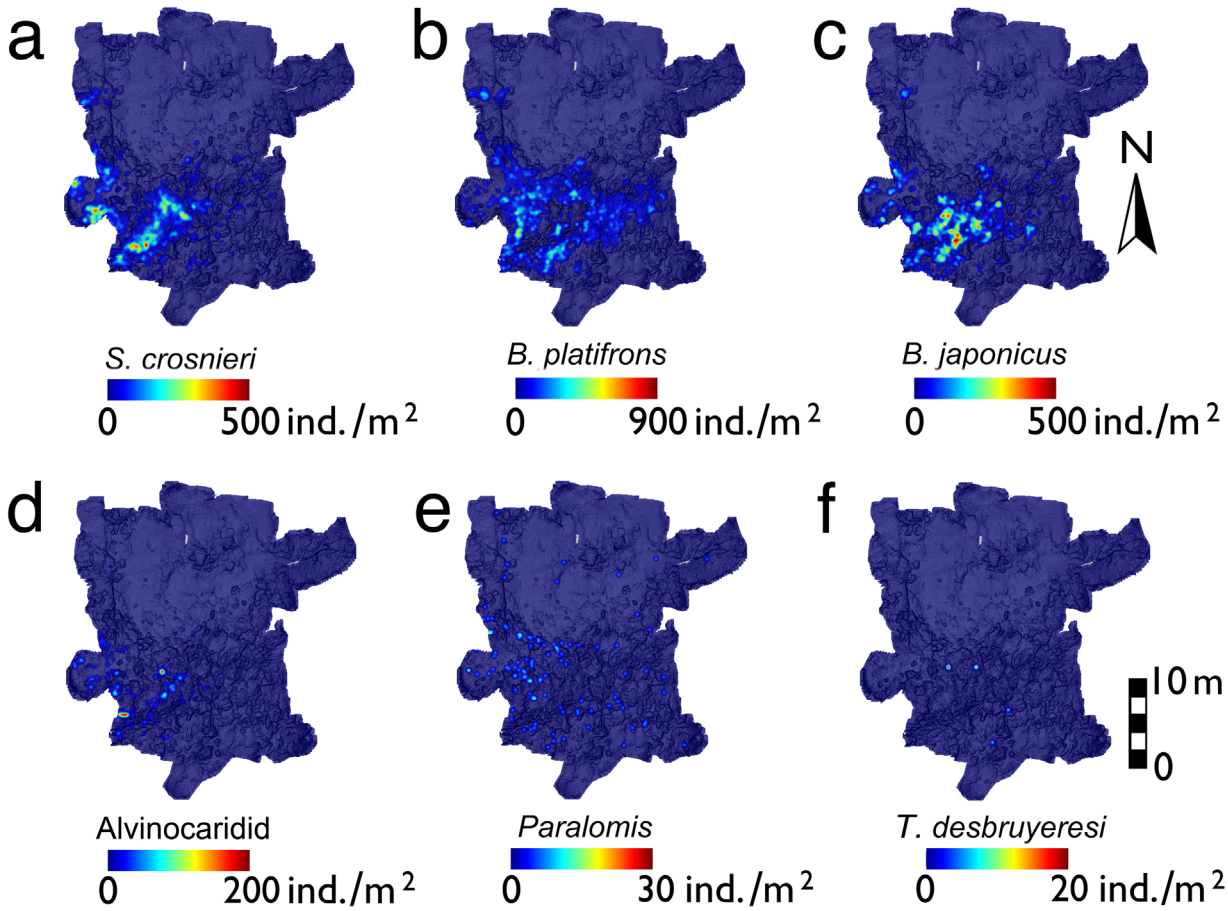

Fig. 9. Population density maps for the NBC_{2m} region. (a) The *S. crosnieri* form dense assemblages, where the highest population density is found on the rocky outcrop located towards the southwest corner of the reconstruction. Both the (b) *B. platifrons* and (c) *B. japonicus* form dense assemblages in the same area of the reconstruction as the *S. crosnieri*. (d) The alvinocaridid shrimp form small assemblages near the larger assemblages of *S. crosnieri* and *Bathymodiolus* mussel on the rocky outcrop. (e) The *Paralomis* are scattered around the reconstruction in areas of both sediment and exposed rocky outcrop with a tendency to be located near areas where there are assemblages of *S. crosnieri* and *Bathymodiolus*. (f) The *T. desbruyeresi* do not form assemblages and are found on the rocky outcrop. (For interpretation of the references to color in the text, the reader is referred to the web version of this article.)

not suffer from perspective errors in areas with rough terrains. However, since visual techniques are limited to surficial counts of resolvable ind., the values of density for taxa that can form multi-layered aggregates, such as the *S. crosnieri* and *Bathymodiolus* mussels, represent minimum estimates of abundance. A further limitation of the proposed method is that even though the reconstruction is performed in 3D, since the images are obtained using vertically downward looking cameras, regions that are steeply sloped or have a rugged terrain, such as the NBC and CBC mounds in NBC_{8m}, are likely to have occlusions in the line of sight of the cameras. This limitation also suggests that the approach describe is likely to underestimate the abundance of ind. in strongly profiled regions. Finally, while the spatial resolution of the reconstructions taken from ~2 m altitude is sufficient to resolve the species >1 cm, poor color contrast with the seafloor in the case of the alvinodaridid and *T. desbruyeresi* may introduce an intrinsic labeling bias that favors the more salient *S. crosnieri*, *Paralomis* and two species of *Bathymodiolus* mussel.

3. Estimation of megabenthic biomass

The 3 representative chemosynthetic species account for more than 97% of the ind. observed in the high-resolution reconstructions (Figs. 11(c) and 12(c)). Considering that the resolution of the reconstructions is <2 mm, it can be reasonably assumed that these 3 species represent almost all the megabenthic biomass of animals >1 cm in size. In order to convert the population density maps into biomass estimates, ind. of the 3 major chemosynthetic species were sampled to determine their total organic carbon (TOC). *S. crosnieri* (173 ind.) were recovered from the NBC and C0014 regions. *B. platifrons* (93 ind.) and *B. japonicus* (11 ind.) were recovered from the NBC region and a region located approximately 50 m southeast of the mound, known as site C0013 (Takai et al., 2011, 2012). Each recovered ind. was weighed and measured along its major axis. No significant difference in size was found between the 2 species of *Bathymodiolus* mussel and so these were combined into a single aggregated set. Of the samples, a representative subset of *S. crosnieri* (11 ind.) and *Bathymodiolus* (13 ind.) were chosen to determine their fractional organic carbon content. The whole bodies of representative ind. were rinsed in filtered seawater, vacuum freeze-dried, and ground into a fine powder. The fine powders were weighed and subjected to further analysis. Either hydrochloric or sulfurous acids were applied as a pretreatment to remove inorganic carbon. After the acid treatment, the % organic carbon content of the subsamples was analysed using an elemental analyzer (Flash EA 1112, Thermo Fisher Scientific). The average and standard deviation of TOC determined for each subset is given in Table 3. These values can be used to determine the distribution of biomass in the high-resolution reconstructions. However, further consideration is necessary to quantify the biomass in the wide-area reconstructions since the *Bathymodiolus* mussels, which account for ~65% of the ind. observed in the high-resolution data, cannot be reliably identified.

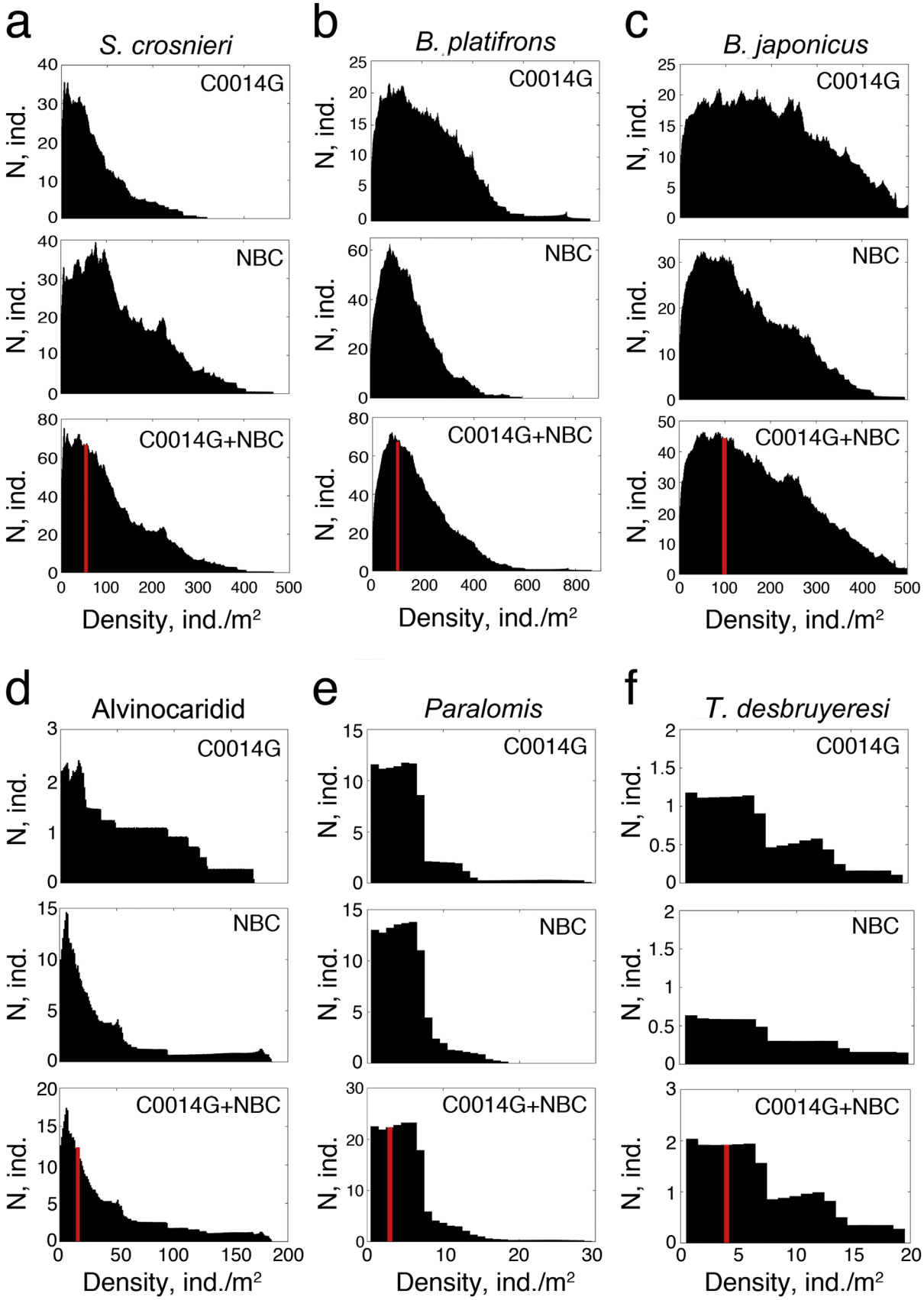

Fig. 10. Histograms of the number of ind. from each taxa observed at a given density in the high-resolution maps. (a) Population density histograms for *S. crosnieri* observed in $C0014G_{2m}$ (top), NBC_{2m} (centre), and combined $C0014G_{2m} \cup NBC_{2m}$ (bottom) regions. (b) Population density histograms for *B. platifrons* observed in $C0014G_{2m}$ (top), NBC_{2m} (centre), and combined $C0014G_{2m} \cup NBC_{2m}$ (bottom) regions. (c) Population density histograms for *B. japonicus* observed in $C0014G_{2m}$ (top), NBC_{2m} (centre), and combined $C0014G_{2m} \cup NBC_{2m}$ (bottom) regions. (d) Population density histograms for alvinocaridid shrimp observed in $C0014G_{2m}$ (top), NBC_{2m} (centre), and combined $C0014G_{2m} \cup NBC_{2m}$ (bottom) regions. (e) Population density histograms for *Paralomis* observed in $C0014G_{2m}$ (top), NBC_{2m} (centre), and combined $C0014G_{2m} \cup NBC_{2m}$ (bottom) regions. (f) Population density histograms for *T. desbruyeresi* observed in $C0014G_{2m}$ (top), NBC_{2m} (centre), and combined $C0014G_{2m} \cup NBC_{2m}$ (bottom) regions. The red lines in the combined data show the density threshold above which more than 68.2% (1σ) of the population of each taxa are observed. (For interpretation of the references to color in this figure legend, the reader is referred to the web version of this article.)

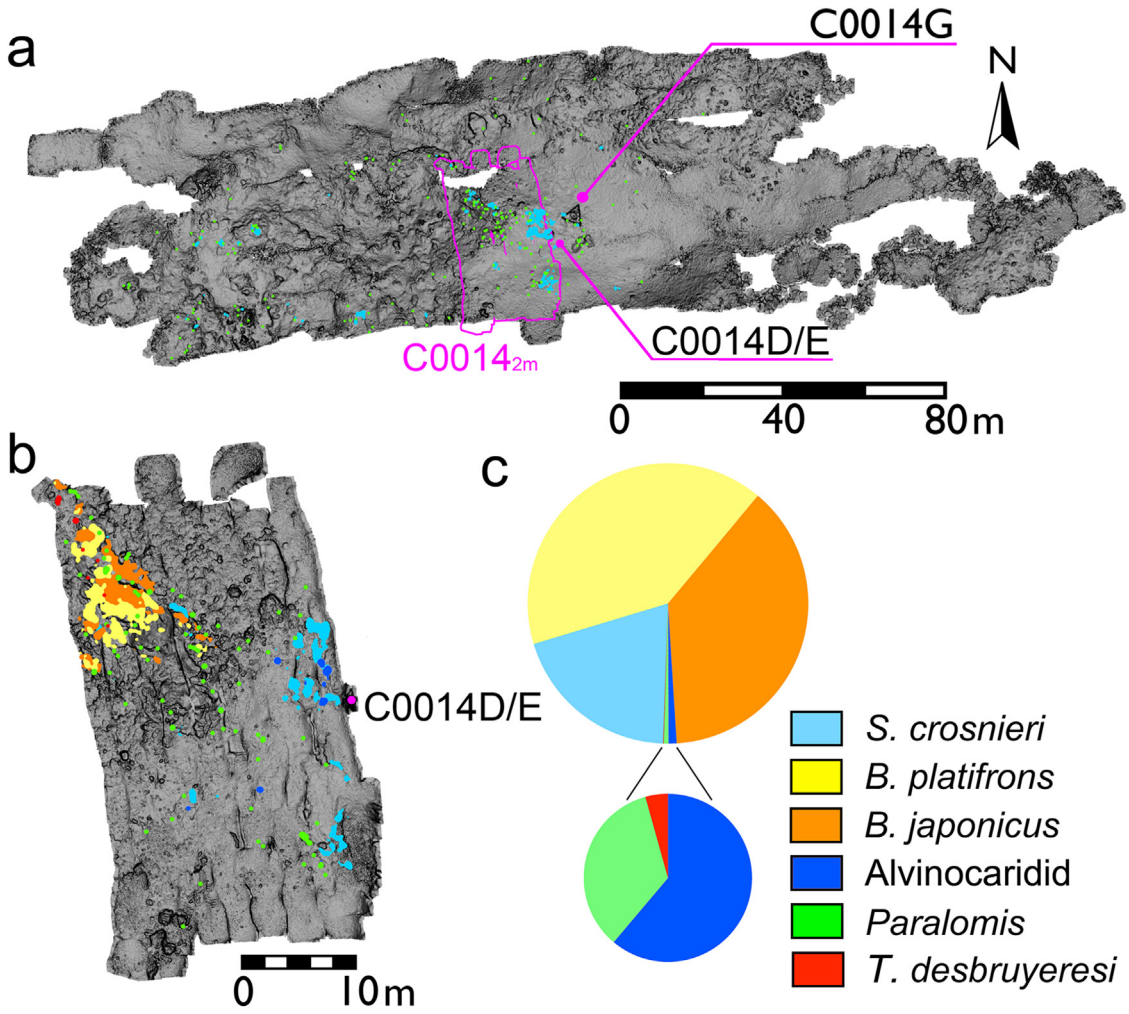

Fig. 11. Distribution of megabenthos in the C0014 region. (a) Distribution of *S. crosnieri* and *Paralomis* identified in the C0014$_{8m}$ region. The purple outline shows the location of the C0014$_{2m}$ region. (b) Distribution of the 6 taxa identified in the C0014$_{2m}$ region. (d) Relative abundance of ind. identified from the different taxa in C0014$_{2m}$. (For interpretation of the references to color in the text, the reader is referred to the web version of this article.)

In this work, the distribution of biomass in the wide-area reconstructions is estimated by using the *Paralomis* as a surrogate. The spatial relationship between the predatory *Paralomis* and the 3 dominant chemosynthetic species is modeled through regression analysis of the high-resolution data (C0014$_{2m}$ and NBC$_{2m}$). Since the distribution of *Paralomis* can be observed over spatial scales of several hectares in the wide-area reconstructions (C0014$_{8m}$ and NBC$_{8m}$) it is possible to apply the modeled relationship to estimate the distribution of megabenthic biomass over the entire seafloor reconstructed in this work.

3.1. Method

To model the relationship between the distribution of *Paralomis* and megabenthic biomass, it is first necessary to express the distribution of the chemosynthetic species in the high-resolution data in terms of their TOC so that the different species can be treated together without biasing the model in favor of larger species. Fig. 13(a) shows the average ratio of megabenthic biomass and *Paralomis* density distribution in the C0014$_{2m}$ and NBC$_{2m}$ regions for different radius Gaussian-weighted convolution windows. For smaller window radii, the density ratios are low since the *Paralomis* are often located several meters away from the nearest chemosynthetic assemblages. However, the ratio begins to converge as the radius of the window increases and a convolution window of radius $\sigma = 5$ m was finally chosen for the model since the ratio is within 5% of the ratio of the total TOC of megabenthos and the number of *Paralomis* observed in the high-resolution maps while still maintaining a high-spatial resolution. Fig. 13(b) shows the relationship between the density of megabenthic biomass and *Paralomis* for the 5 m σ radius convolution window. The plot shows that while the NBC$_{2m}$ region has higher densities of biomass and *Paralomis*, both C0014$_{2m}$ and NBC$_{2m}$ follow the same trend even though the two regions are located ~450 m apart. The regression model was derived by applying an ordinary least square fit to a power relationship of the form $y = ax^b$, where the coefficients $a = 308.6$ and $b = 1.663$ provided the best fit to the data. Fig. 13(b) shows the derived regression curve as a solid line together with the 95% confidence interval shown by the shaded region. The predictive accuracy of the model is assessed using a Monte-Carlo cross-validation technique that consists of 3,000 randomly split sets of independent training and test data extracted from the high-resolution reconstructions (Picard and Cook, 1984). For each split, the model was fit to the training data and used to predict megabenthic biomass in an independent test set based on the distribution of *Paralomis*. Independent training and test data were ensured for each split by restricting the test data to ind. located more than 5 m away from any member of the corresponding training data. Fig. 14 shows a normalised histogram of the relative error for the 3,000 randomly generated sets. The mean relative

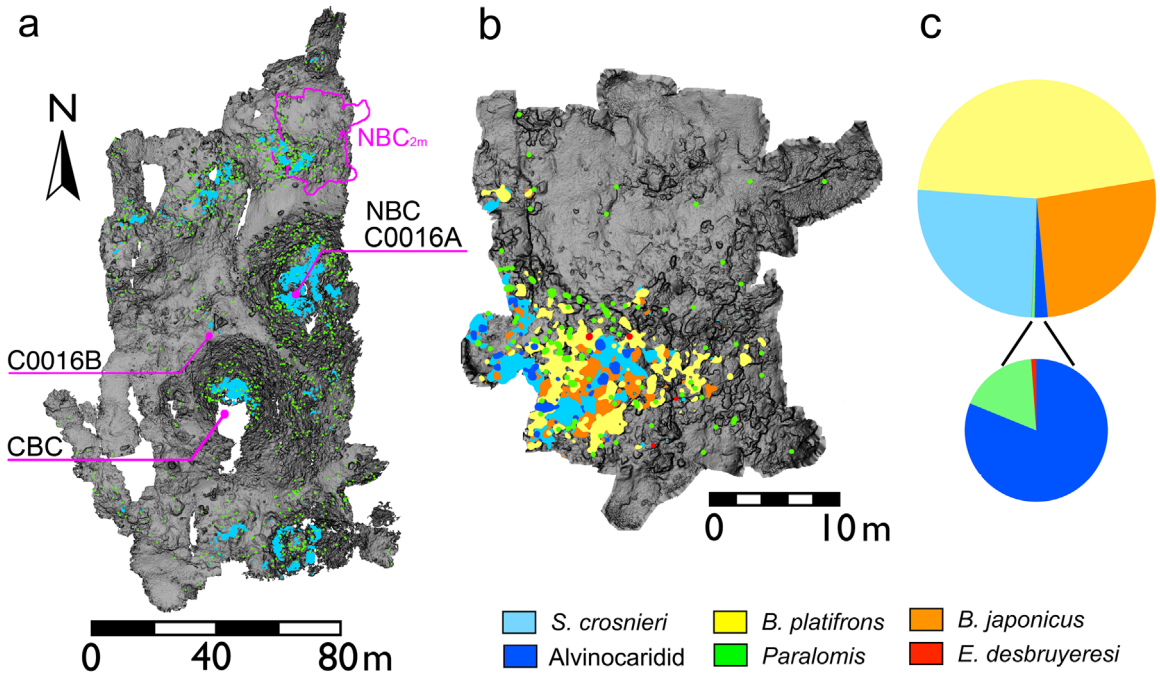

Fig. 12. Distribution of megabenthos in the NBC region. (a) Distribution of *S. crosnieri* and *Paralomis* identified in the NBC_{8m} region. The purple outline shows the location of the NBC_{2m} region. (b) Distribution of the 6 taxa identified in the NBC_{2m} region. (d) Relative abundance of ind. identified from the different taxa in NBC_{2m}. (For interpretation of the references to color in the text, the reader is referred to the web version of this article.)

Table 3
Analysis of biological samples. The samples were collected from the survey area. The average and standard deviations for shell length and mass are determined from measurement made on all ind. recovered from each taxon. The average and standard deviation of total organic carbon (TOC) are determined from the fractional organic carbon content of a representative subset of *S. crosnieri* (11 ind.) and *Bathymodiolus* (13 ind.).

	S. crosnieri	*Bathymodiolus*
No. samples	173	108
Shell major Axis length, mm	35.8 ± 7.8	53.2 ± 26.2
Mass, g	3.0 ± 0.5	15.6 ± 8.8
TOC, g C	0.90 ± 0.14	0.40 ± 0.11

error is $< 1\%$ and the uncertainty of the model used for the conversion is determined as 21.1% based on the standard deviation of the relative prediction error.

In order to apply this relationship to the wide-area reconstructions, it is necessary to account for systematic errors in the identification of ind. mapped at the lower-resolution. This is characterised based on the number of ind. observed in overlapping regions of the reconstructions generated from the different altitudes. For this, it is important that the position error between the overlapping reconstructions is small. A relative position error of < 0.1 m is achieved by aligning the individual reconstructions taken from different altitudes using the Georeferencer tool in qGIS by manually identifying visual features that are common between the different resolution reconstructions, where the high-resolution reconstructions are translated and rotated to be consistent with the wide-area data. It is also necessary to assume that the net movement of ind. across the boundaries of the overlapping areas between reconstructions is negligible. This is reasonable since the duration of the survey is short compared to the time scales on which the underlying processes that sustain the benthos are expected to vary (Copley et al., 1999; Kawagucci et al., 2013; Nakajima et al., 2015). Subject to these conditions, the low-altitude reconstructions can be used as a basis for comparison. The counting uncertainty for the wide-area reconstructions is determined to be 16.3% for the *Paralomis* in the overlapping regions $C0014_{2m} \cap C0014_{8m}$ and $NBC_{2m} \cap NBC_{8m}$, illustrated by the purple outlines in Figs. 15(a), (b) and 16(a) and (b), respectively. This is less than the conversion model uncertainty and the propagated counting and conversion errors give a total biomass estimation uncertainty of 26.7%, which is considered acceptable for the purpose of this research.

3.2. Results

The estimated distribution of megabenthic biomass in the $C0014_{8m}$ and NBC_{8m} regions are shown in Figs. 15 and 16, respectively. Figs. 15(a) and 16a show the distributions of *S. crosnieri* in units of g C/m^2 that were determined from direct observation in the high-altitude reconstructions. Here a value of 0.90 ± 0.14 g C/ind., determined from sampled ind., was used where a counting uncertainty of 33.5% was introduced based on the number of *S. crosnieri* observed in the overlapping regions $C0014_{2m} \cap C0014_{8m}$ and $NBC_{2m} \cap NBC_{8m}$. Figs. 15(b) and 16(b) show the distribution of biomass estimated from the *Paralomis* identified in the wide-area reconstructions as determined using the method described in Section 3.1. Table 4 summarises the parameters used to convert the wide-area reconstructions into estimates of biomass together with their uncertainties.

The accuracy of the estimated biomass is evaluated through comparison with the distribution of biomass calculated from direct observations of *S. crosnieri* and *Bathymodiolus* mussels in the overlapping regions of the high-resolution data $C0014_{2m} \cap C0014_{8m}$ and $NBC_{2m} \cap NBC_{8m}$. Fig. 15(c) and (d) shows the *S. crosnieri* biomass determined through direct observation in the wide-area reconstructions and the megabenthic biomass estimated based on the distribution of *Paralomis* in the overlapping region $C0014_{2m} \cap C0014_{8m}$. Fig. 15(e) shows the corresponding distribution of biomass calculated based on the direct observations made in the high-resolution data. Fig. 16(c)–(e) shows the

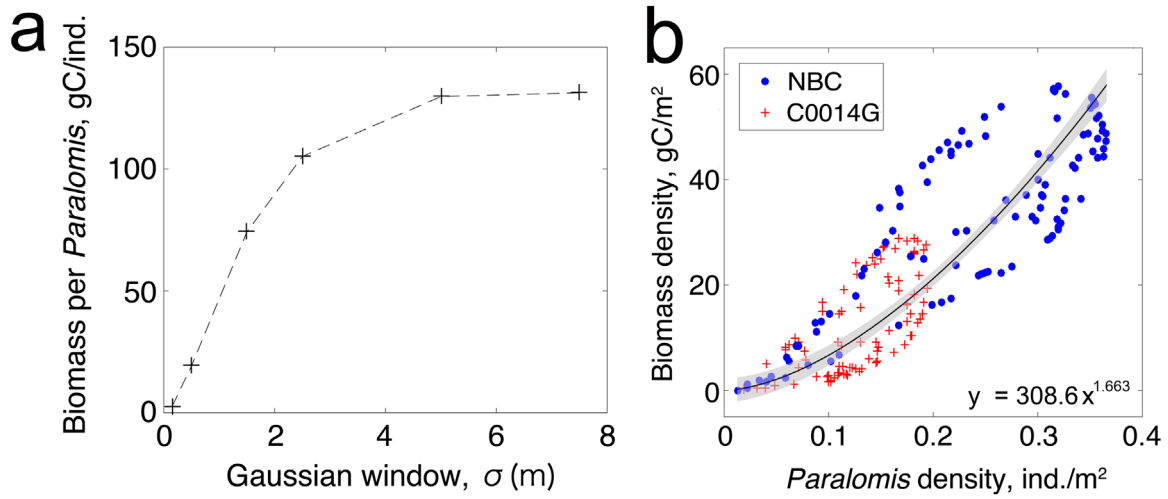

Fig. 13. Relationship between megabenthic biomass and *Paralomis* in the $C0014_{2m}$ and NBC_{2m} regions. (a) Ratio of megabenthic biomass and *Paralomis* densities as a function of the radius of the Gaussian-shaped convolution operator used to determine each density. The plot shows the average values determined for all *Paralomis* ind. in both regions. (b) Density of megabenthic biomass as a function of *Paralomis* density for a Gaussian-shaped convolution operator with a σ radius of 5 m. The solid line shows the non-linear regression that was derived by applying an ordinary least square fit to a power relationship of the form $y=ax^b$, where the coefficients a=308.6 and b=1.663 provided the best fit to the data. The shaded region shows the 95% confidence interval of the model. (For interpretation of the references to color in the text, the reader is referred to the web version of this article.)

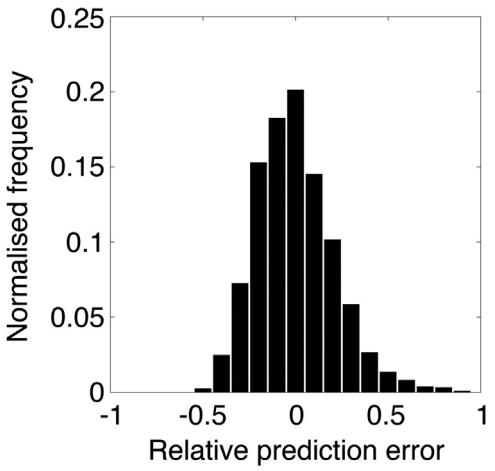

Fig. 14. Relative prediction error of the modeled relationship between the density of megabenthic biomass and *Paralomis* in the $C0014_{2m}$ and NBC_{2m} regions. The histogram shows the relative error for 3,000 randomly selected sets of independent training and test data.

equivalent data for the overlapping region $NBC_{2m} \cap NBC_{8m}$. The abundance and maximum density of biomass in each of the reconstructions are summarised in Table 5 together with bounded uncertainty estimates for each of the different methods used. The TOC of *S. crosnieri* in the overlapping regions observed in the wide-area reconstructions account for just 28% and 40% of the respective values of abundance and maximum density of biomass determined from the distribution of chemosynthetic species in the overlapping regions of the high-resolution data. The relative proportions of biomass and density described by the *S. crosnieri* are different since their spatial distribution differs from the *Bathymodiolus* mussels that make up a significant portion of the total biomass. This implies that the distribution of *S. crosnieri* is not a reliable indicator of biomass since even if a correction factor is introduced to correct for the relative abundance that the *S. crosnieri* account for, this would not necessarily translate to a sensible prediction of the distribution and density of biomass. This can be seen in Fig. 15(e) where the location of the maximum density of *S. crosnieri* (blue marker) in the wide-area reconstructions is located 18.5 m from the maximum density of biomass (purple marker) determined from the high-resolution data. For the data described in this study, a correction factor based on abundance would result in a significant over prediction of the maximum biomass density and would also not accurately describe biomass distribution. It is noted however, that the difference in the distribution patterns observed between the *S. crosnieri* and *Bathymodiolus* are most noticeable near post-drilling hydrothermal discharges in sediment-covered areas. Therefore, it is possible that the distribution patterns observed in this study are unique to areas that have been perturbed by anthropogenic drilling activity. The megabenthic biomass estimates made based on the distribution of *Paralomis* in the wide-area reconstructions account for 99% and 94% of the respective values of abundance and maximum density of biomass in the overlapping regions of the high-resolution data. Figs. 15 (e) and 16(e) show that the location of the maximum biomass density determined from the distribution of *Paralomis* (green markers) in the overlapping areas differs from those observed in the high-resolution data (purple markers) by straight-line distances of 8.6 and 5.2 m respectively. The discrepancy in location of the predicted maximum biomass density is reasonable considering the σ=5 m radius of the Gaussian-shaped convolution window used in the model. The validation demonstrates that regression based on *Paralomis* distribution can estimate the distribution and amount of megabenthic biomass within the derived limits of uncertainty.

4. Discussion

The abundance and maximum density of megabenthic biomass in the $C0014_{8m}$ and NBC_{8m} regions surveyed in this study are summarised in Table 5. The megabenthic biomass in the $C0014_{8m}$ region determined from the distribution of *Paralomis* is 25 ± 7 kg C over a projected horizontal surface area of 1.3 ha. The maximum biomass density is determined to be 27 ± 7 g C/m^2 and is located in the area that was intensively drilled during the IODP 331 expedition (Figs. 3(c) and 15(b) and (e)). The majority of the remaining biomass is located toward the west of the surveyed region, where the highest biomass densities are $\sim 5 \pm 2$ gC/m^2. The density of biomass near the drill-site is significantly higher than in

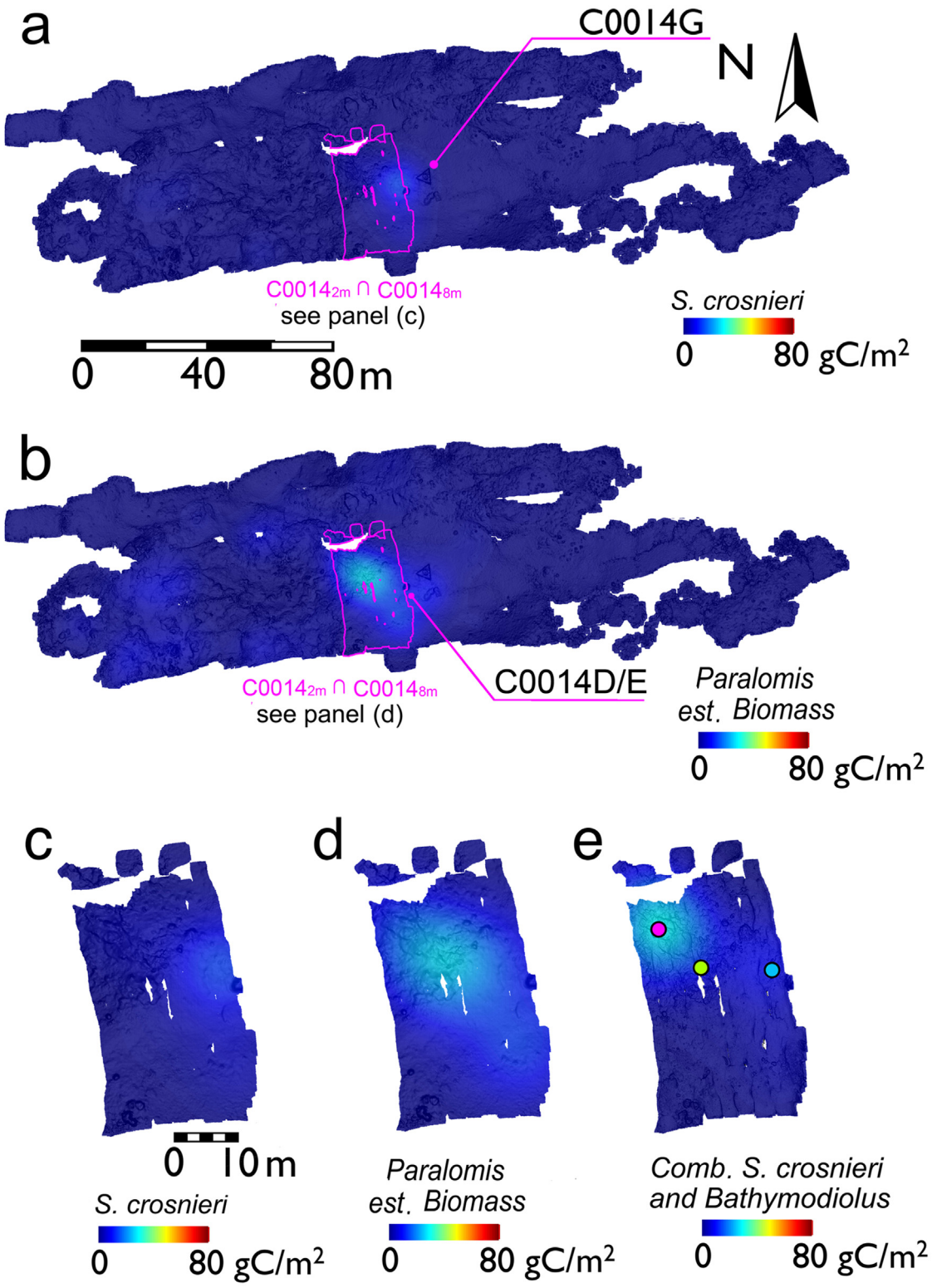

Fig. 15. Distribution of megabenthic biomass in the C0014 region. (a) *S. crosnieri* biomass determined from direct observation of ind. in the C0014$_{8m}$ reconstruction. (b) Megabenthic biomass estimated from the distribution of *Paralomis* in the C0014$_{8m}$ reconstruction. The purple outline shows the overlapping region of the wide-area C0014$_{8m}$ and high-resolution C0014$_{2m}$ reconstructions. (c) Detailed view of *S. crosnieri* biomass distribution shown in (a) for the overlapping region C0014$_{2m}$ ∩ C0014$_{8m}$. (d) Detailed view of estimated megabenthic biomass distribution shown in (b) for the C0014$_{2m}$ ∩ C0014$_{8m}$ region. (e) Megabenthic biomass distribution determined from direct observations in the C0014$_{2m}$ reconstruction for the C0014$_{2m}$ ∩ C0014$_{8m}$ region. The purple marker in (e) shows the location of the maximum density of biomass observed in the high-resolution data, the blue marker shows the location of the maximum density of *S. crosnieri* observed in C0014$_{8m}$ and the green marker shows the location of the maximum biomass estimated from the distribution of *Paralomis* in C0014$_{8m}$. A 5 m radius Gaussian-shaped convolution operator is used for all calculation made. A 5 m radius Gaussian-shaped convolution operator was used when determining the distributions shown in this figure. (For interpretation of the references to color in this figure legend, the reader is referred to the web version of this article.)

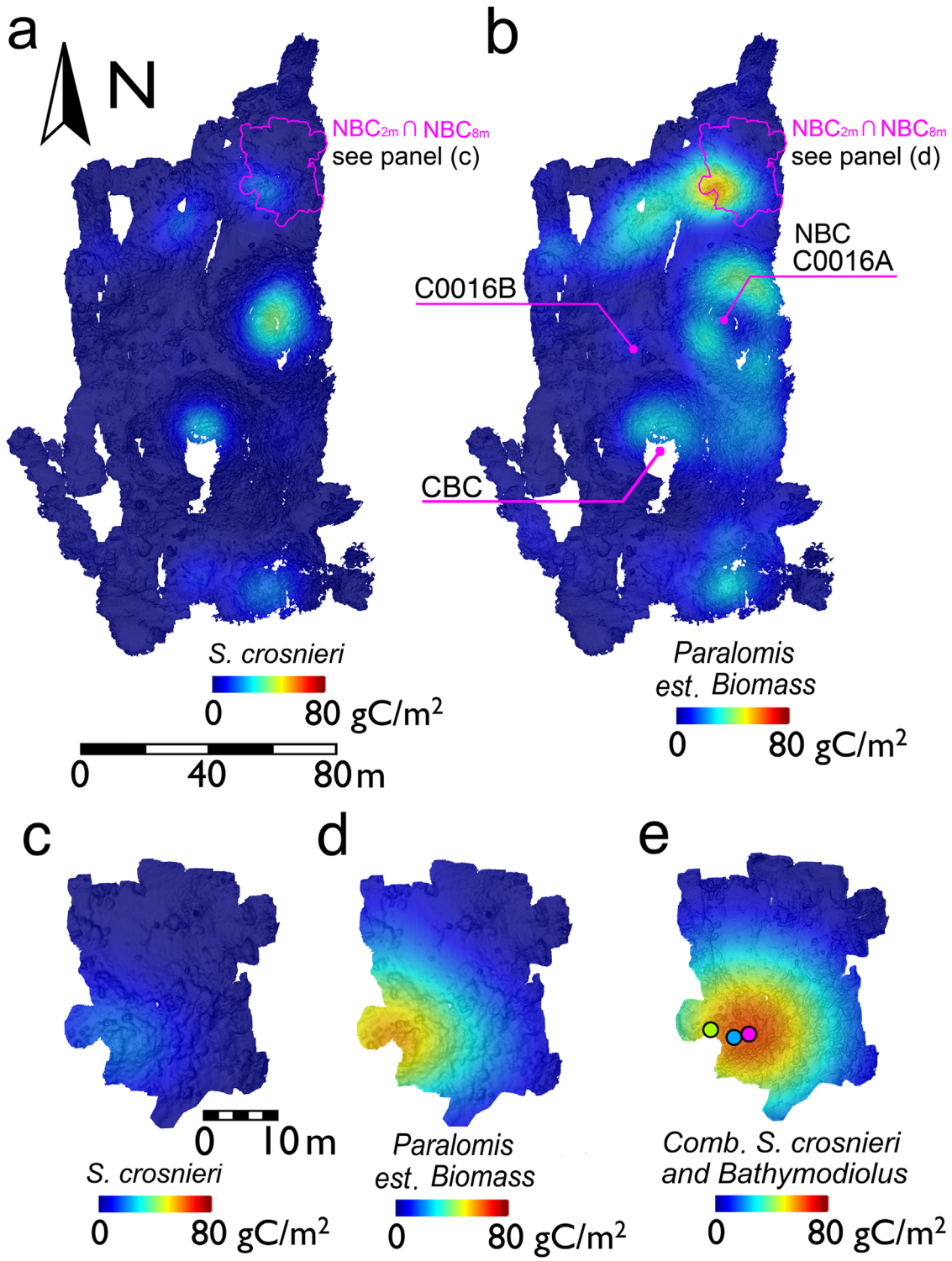

Fig. 16. Distribution of megabenthic biomass in the NBC region. (a) *S. crosnieri* biomass determined from direct observation of ind. in the NBC_{8m} reconstruction. (b) Megabenthic biomass estimated from the distribution of *Paralomis* in the NBC_{8m} reconstruction. The purple outline shows the overlapping region of the wide-area NBC_{8m} and high-resolution NBC_{2m} reconstructions. (c) Detailed view of *S. crosnieri* biomass distribution shown in (a) for the overlapping region $NBC_{2m} \cap NBC_{8m}$. (d) Detailed view of estimated megabenthic biomass distribution shown in (b) for the $NBC_{2m} \cap NBC_{8m}$ region. (e) Megabenthic biomass distribution determined from direct observations in the NBC_{2m} reconstruction for the $NBC_{2m} \cap NBC_{8m}$ region. The purple marker in (e) shows the location of the maximum density of biomass observed in the high-resolution data, the blue marker shows the location of the maximum density of *S. crosnieri* observed in NBC_{8m} and the green marker shows the location of the maximum biomass estimated from the distribution of *Paralomis* in NBC_{8m}. A 5 m radius Gaussian-shaped convolution operator was used when determining the distributions shown in this figure. (For interpretation of the references to color in this figure legend, the reader is referred to the web version of this article.)

other areas in the $C0014_{8m}$ region. Biomass densities >7 g C/m^2 are localised to within a 20 m radius of drilled area. While it is known that the region within a 15 m radius of the drilled area was not inhabited before drilling, it has been reported in Nakajima et al. (2015) that some *S. crosnieri* and *Bathymodiolus* mussel assemblages were present in the rocky area ~20 m west of the area that was drilled. As such, it is not possible to determine the amount of biomass that can be directly attributed to post-drilling

discharge since the number of ind. in this area prior to drilling is not known. However, at the time of the survey the drilled area supported a large megabenthic assemblage of 11 ± 3 kg C that covered an area of 560 m^2, corresponding to an average density of 19 ± 5 g C/m^2. This forms an upper limit for the effects of post-drilling discharge in this area. The abundance of megabenthic biomass in the highly active NBC_{8m} region is 140 ± 40 kg C over a projected horizontal surface area of 1.2 ha. Both the abundance of biomass and the average density per unit area are more than 5 times those of the $C0014_{8m}$ region. The drill-holes in this region are located at the C0016B guide base and C0016A located on top of the NBC mound. Large assemblages of biomass are also found on several mounds that have not been drilled. The maximum density of biomass observed on the NBC mound is 33 ± 9 g C/m^2. It is known that the NBC mound was densely populated by megabenthos before hole C0016A was drilled (Watanabe et al., 2010; Kawagucci et al., 2013). However, since the abundance and density of biomass prior to drilling are not known it is not clear what portion of the observed biomass can be attributed to the effects of drilling. The maximum density of biomass on the NBC mound however, is not significantly different from the densities on the other mounds in this region that have not been drilled, which range from 22 ± 6 to 56 ± 15 g C/m^2. The C0016B guide base is located in a small area covered by sediments located 30 m west of the C0016A hole at the base of the NBC and CBC mounds. Inspection of Fig. 4(a) shows white sediments, possibly originating from drill cuttings, extending 15 m east of the C0016B hole forming a layer of deposit of unknown thickness. Fig. 12(a) shows that there is a small assemblage of *S. crosnieri* at the southwest corner of the guide base and a small number of *Paralomis*. The estimated maximum density of biomass in this area is 7 ± 2 g C/m^2 where the increased density is confined to within 7 m of the centre of C0016B. The highest density of megabenthic biomass in the NBC_{8m} region is found 40 m north of the NBC mound on top of a 6 m high mound that has a diameter of 20 m. This area partially overlaps with the high-resolution NBC_{2m} reconstruction and is characterised by visible diffuse flow. No drilling has been performed on this mound and the high density of biomass (56 ± 15 g C/m^2) observed can be attributed to naturally occurring hydrothermal discharge.

This study provides insight into the effects on megabenthos (> 1 cm) of drilling in hydrothermally active areas. Drilling activities in the C0014 region of the Iheya North field, consisting of seven holes that were drilled within a 10 m radius and to maximum drill depth of 137.6 mbsf, have generated post-drilling hydrothermal discharges that sustain an assemblage of *S. crosnieri* more than 3 years and 4 months after the site was drilled (Kawagucci et al., 2013; Nakajima et al., 2015). The seafloor surrounding the drill-site supports a diverse assemblage of megabenthos that is confined to an area of diameter 20 m centered around the drill-holes, with no noticeable affect on the distribution of biomass in the surrounding 1.3 ha region. While it has been suggested that a large proportion of this biomass may be attributed to post-drilling hydrothermal discharge (Nakajima et al., 2015), the projected area, abundance and maximum density of the assemblage are smaller than those observed in the natural assemblages in the nearby NBC region, where the maximum density of biomass near the C0014 drill-site is approximately half of the density observed in the most active area of the NBC region. Drilling activities in the region surrounding the NBC mound were less extensive than at the C0014 drill-site. While a small assemblage of $< 0.5 \pm 0.1$ kg C was observed < 7 m from the C0016B hole, the density of biomass here is less than one-third of that observed on adjacent mounds that were not drilled. Similarly, no significant difference was observed in the density of biomass on the NBC mound, where the C0016A hole was drilled, compared to adjacent mounds that have not been drilled.

Table 4
Functions used to estimate the distribution of biomass from the observed distributions of *Paralomis* and *S. crosnieri*, respectively. The input variable x is the density distribution of each respective taxon as determined using a 5 m radius Gaussian-shaped convolution operator. The conversion function for *S. crosnieri* corresponds to the TOC of recovered ind. given in Table 3. The conversion function for *Paralomis* corresponds to the regression curve shown in Fig. 13(b).

Species	Conversion function	Model uncertainty, %		
		Counting	Conversion	Total
S. crosnieri	0.90x	33.5	< 0.1	33.5
Paralomis	$308.6x^{1.663}$	16.3	21.1	26.7

5. Conclusions

This study is the first multi-hectare scale survey of the quantitative distribution of a vent-endemic megabenthic community. This was achieved through the application of a novel multi-resolution 3D reconstruction technique and the use of surrogate taxa that can rapidly survey multi-hectare regions of the seafloor using an appropriately instrumented underwater robot. The method is practical and can be used to survey deep-sea benthic ecosystems on spatial scales that could not previously be studied. The technique was applied to investigate the post-drilling response of megabenthic communities in the Iheya North field. The data forms the largest spatially continuous dataset for vent ecology and the results find that, 3 years and 4 months after the drilling activities of the IODP 331 expedition, the effects of post-drilling discharge

Table 5
Abundance and maximum density of biomass determined for each of the surveyed areas. The biomass determined for the high-resolution reconstructions is based on direct observations of *S. crosnieri* and *Bathymodiolus* mussel ind. where the values of TOC in Table 3 have been used to convert the population densities into biomass estimates. The biomass estimated from the wide-area reconstruction is computed based on the conversion functions in Table 4. A 5 m radius Gaussian-shaped convolution operator is used for all calculation made.

Region	Biomass from high-resolution reconstructions			Biomass from wide-area reconstructions		
	Method	Abundance, kg C	Max. density, g C/m^2	Method	Abundance, kg C	Max. density, g C/m^2
$C0014_{2m} \cap C0014_{8m}$	*Combined S. cronieri and Bathymodulii*	7.94 ± 0.01	30.0 ± 0.1	*S. crosnieri*	2.7 ± 0.9	14 ± 5
				Paralomis	8.6 ± 2.3	27 ± 7
$NBC_{2m} \cap NBC_{8m}$	*Combined S. cronieri and Bathymodulii*	13.24 ± 0.01	57.6 ± 0.1	*S. crosnieri*	2.9 ± 1.0	19 ± 6
				Paralomis	12 ± 3	56 ± 15
$C0014G_{8m}$	–	–	–	*S. crosnieri*	5.7 ± 1.9	14 ± 5
				Paralomis	25 ± 7	27 ± 7
NBC_{8m}	–	–	–	*S. crosnieri*	42 ± 14	39 ± 13
				Paralomis	140 ± 40	56 ± 15

on the distribution of megabenthos in the surveyed regions has remained bounded to spatial scales of several tens of meters from the drill-holes. While it is difficult determine the extent to which the observed distributions can be attributed to drilling activity, the density of megabenthos in the drilled areas are found to be within the order that is associated with naturally occurring hydrothermal discharges in this region. It is important to recognise however that drilling activities may potentially redirect vent fluid away from existing discharge channels and so biomass in these areas may decrease. However, it is not known over what spatial or temporal scales these effects may occur.

Some unique characteristics have been observed regarding the influence on the local distribution of megabenthos. In particular, the areas surrounding the C0014G and C0016B holes are the only locations where *S. crosnieri* were observed on flat, sediment-covered terrains. All other assemblages of *S. crosnieri* identified in the 2.5 ha of seafloor that was surveyed were found on rocky outcrops. This may be because in this region, naturally occurring hydrothermal discharges are usually accompanied by the formation of mineral deposits. However, the drill-holes made during the IODP 331 expedition penetrated some distance into the base rock in sediment-covered areas (Takai, 2011, 2012) and have resulted in the sustained discharge of hydrothermal fluids. This has attracted assemblages of *S. crosnieri* to sediment-covered areas, which now support vent communities with a unique structure. While this study has found the effects of drilling in the Iheya North field on the distribution of megabenthos to be bounded to within naturally occurring levels, some changes in distribution have been observed and it is not clear how these effects would scale with more extensive drilling or how the changes observed will evolve with time. It is clear that potential changes in benthic communities need to be considered when planning drilling activities in hydrothermally active areas and that these activities should be supported by appropriate efforts in monitoring.

Acknowledgments

This work was funded in part by the Japan Science and Technology CREST grant program for the “Establishment of core technology for the preservation and regeneration of marine biodiversity and ecosystems” and the Australia-Japan Foundation Grant no. G176443.

References

Bach, W., Edwards, K.J., 2003. Iron and sulfide oxidation within the basaltic ocean crust: extent, processes, timing, and implications for chemolithoautotrophic primary biomass production. Geochim. Cosmochim. Acta 67, 3871–3887.

Bachraty, C., Legendre, P., Desbruyères, D., 2009. Biogeographic relationships among deep-sea hydrothermal vent faunas at global scale. Deep Sea Res. 56, 1371–1378.

Bergquist, D.C., Eckner, J.T., Urcuyo, I.A., Cordes, E.E., Hourdez, S., Macko, S.A., Fisher, C.R., 2007. Using stable isotopes and quantitative community characteristics to determine a local hydrothermal vent food web. Mar. Ecol. Prog. Ser. 330, 49–65.

Bodenmann, A., Thornton, B., Ura, T., 2010. 3D mapping of the seafloor in color using a single camera. Sea Technol. 51, 51–53.

Bodenmann, A., Thornton, B., Ura, T., 2016. Generation of high-resolution 3D reconstructions of the sea floor in colour using a single camera and structured light. J. Field Robot. http://dx.doi.org/10.1002/rob.21682

Bodenmann, A., Thornton, B., Ura, T., 2013. Development of long range color imaging for wide area 3D reconstruction of the seafloor, In: Proceedings of the Underwater Tech. Symp., Tokyo, Japan.

Bodenmann, A., Thornton, B., Ura, T., 2014. Visual 3D mapping to measure hydrothermal deposit growth rates at a man-made deep sea vent, In: Proceedings of the AUV 2014, Mississippi, US.

Connelly, D.P., Copley, J.T., Murton, B.J., Stansfield, K., Tyler, P.A., German, C.R., Van Dover, C.L., Amon, D., Furlong, M., Grindlay, N., Hayman, N., Hühnerbach, V., Judge, M., Le Bas, T., McPhail, S., Meier, A., Nakamura, K., Nye, V., Pebody, M., Pedersen, R.B., Plouviez, S., Sands, C., Searle, R.C., Stevenson, P., Taws, S., Wilcox, S., 2012. Hydrothermal vent fields and chemosynthetic biota on the World's deepest seafloor spreading centre. Nat. Commun. 3, 620.

Copley, J.T.P., Tyler, P.A., Van Dover, C.L., Schultz, A., Dickson, P., Singh, S., 1999. Subannual temporal variation in faunal distributions at the TAG hydrothermal mound (26N, Mid-Atlantic Ridge). PSZN: Mar. Ecol. 20, 291–306.

Corliss, J.B., Dymond, J., Gordon, L.I., Edmond, J.M., von Herzen, R.P., Ballard, R.D., Green, K., Williams, D., Bainbridge, A., Crane, K., van Andel, T.H., 1979. Submarine thermal springs on the Galapagos Rift. Science 203, 1073–1083.

Cowen, J.P., Giovannoni, S.J., Kenig, F., Johnson, H.P., Butterfield, D., Rappé, M.S., Hutnak, M., Lam, P., 2003. Fluids from aging oceanic crust that support microbial life. Science 299, 120–123.

Dansereau, D.G., Williams, S.B., 2011. Seabed modeling and distractor extraction for mobile AUVs using light field filtering. In: Proceedings of the 2011 IEEE International Conference on Robotics and Automation (ICRA), Shanghai, China, pp. 1634–1639.

Desbruyères, D., Almeida, A., Biscoito, M., Comtet, T., Khripounoff, A., Le Bris, N., Sarradin, P.M., Segonzac, M., 2000. A review of the distribution of hydrothermal vent communities along the northern Mid-Atlantic Ridge dispersal vs. environmental controls. Hydrobiologia 440, 201–216.

Escartin, J., García, R., Delaunoy, O., Ferrer, J., Gracias, N., Elibol, A., Cufi, X., Neumann, L., Fornari, D.J., Humphris, S.E., Renard, J., 2008. Globally aligned photomosaic of the Lucky Strike hydrothermal vent field (Mid-Atlantic Ridge, 37°18.5°N): release of georeferenced data, mosaic construction, and viewing software. Geochem. Geophys. Geosyst. 9, Q12009.

Fisher, C.R., Childress, J.J., Macko, S.A., Brooks, J.M., 1994. Nutritional interactions in Galapagos rift hydrothermal vent communities: inferences from stable carbon and nitrogen isotope analyses. Mar. Ecol. Prog. Ser. 103, 45–55.

Fujikura, K., Hashimoto, J., Okutani, T., 2002. Estimated population densities of Megafauna in two chemosynthesis based communities: a cold seep in Sagami Bay and a hydrothermal vent in the Okinawa Trough. Benthos Res. 57, 21–30.

Fujiwara, Y., Takai, K., Uematsu, K., Tsuchida, S., Hunt, J.C., Hashimoto, J., 2000. Phylogenetic characterization of endosymbionts in three hydrothermal vent mussels: influence on host distributions. Mar. Ecol. Prog. Ser. 208, 147–155.

Garcia, R., Campos, R., Escartin, J., 2011. High-resolution 3D reconstruction of the seafloor for environmental monitoring and modelling. In: Proceedings of the 2011 IEEE/RSJ Intelligent Robots and Systems (IROS), San Francisco, USA, pp. 58–65.

Gena, K., 2013. Deep sea mining of submarine hydrothermal deposits and its possible environmental impact in Manus Basin, Papua New Guinea. Procedia Earth Plan. Sci. 6, 226–233.

Glover, A.G., Smith, C.R., 2003. The deep-sea floor ecosystem: current status and prospects of anthropogenic change by the year 2025. Environ. Conserv. 30, 219–241.

Hannington, M.D., Jamieson, J.J., Monecke, T., Petersen, S., Beaulieu, S., 2011. The abundance of seafloor massive sulfide deposits. Geology 39, 1155–1158.

Hannington, M.D., Jonasson, I.R., Herzig, P.M., Petersen, S., 1995. Physical and chemical processes of seafloor mineralization at mid-ocean ridges. In: Humphris, S. E., Zierenberg, R.A., Mullineaux, L.S., Thomson, R.E., (Eds.), Seafloor Hydrothermal Systems: Physical, Chemical, Biological and Geological Interactions. AGU Geophys. Mono. Ser., vol. 91, pp. 115–157.

Hashimoto, J., Okutani, T., 1994. Four new mytilid mussels associated with deepsea chemosynthetic communities around Japan. Venus 53, 61–83.

Inglis, G., Smart, C., Vaughn, I., Roman, C., 2012. A pipeline for structured light bathymetric mapping. In: Proceedings of the 2012 IEEE/RSJ International Conference on Intelligent Robots and Systems (IROS), Vilamoura-Algarve, Portugal, pp. 4425–4432.

Jalving, B., 1999, Depth accuracy in seabed mapping with underwater vehicles, In: Proceedings of the 2009 MTS/IEEE Oceans, Seattle, USA, pp. 973–978.

Jannasch, H.W., Mottl, M.J., 1985. Geomicrobiology of deep-sea hydro-thermal vents. Science 229, 717–725.

Jannasch, H.W., Nelson, D.C., Wirsen, C.O., 1989. Massive natural occurrence of unusually large bacteria (Beggiatoa) at a hydrothermal deep-sea vent site. Nature 342, 834–836.

Johnson, K.S., Childress, J.J., Beehler, C.L., Sakamoto, C.M., 1994. Biogeochemistry of hydrothermal vent mussel communities: the deep-sea analogue to the intertidal zone. Deep Sea Res. 41, 993–1011.

Johnson-Roberson, M., Pizarro, O., Williams, S.B., Mahon, I., 2010. Generation and visualization of large-scale three-dimensional reconstructions from underwater robotic surveys. J. Field Robot. 27, 21–51.

Juniper, S.K., Jonasson, I.R., Tunnicliffe, V., Southward, A.J., 1992. Influence of tube-building polychaete on hydrothermal chimney mineralization. Geology 20, 895–898.

Kawagucci, S., Miyazaki, J., Nakajima, R., Nozaki, T., Takaya, Y., Kato, Y., Shibuya, T., Konno, U., Nakaguchi, Y., Hatada, K., Hirayama, H., Fujikura, K., Furushima, Y., Yamamoto, H., Watsuji, T., Ishibashi, J., Takai, K., 2013. Post-drilling changes in fluid discharge pattern, mineral deposition, and fluid chemistry in the Iheya North hydrothermal field, Okinawa Trough. Geochem. Geophys. Geosyst. 14, 4774–4790.

Kim, S., Hammerstrom, K., 2012. Hydrothermal vent community zonation along environmental gradients at the Lau back-arc spreading center. Deep Sea Res. I 62, 10–19. http://dx.doi.org/10.1016/j.dsr.2011.12.010.

Kremen, C., 1992. Assessing the indicator properties of species assemblages for natural areas monitoring. Ecol. Appl. 2, 203–217.

Kwasnitschka, T., Köser, K., Sticklus, J., Rothenbeck, M., Weiß, T., Wenzlaff, E., Schoening, T., Triebe, L., Steinführer, A., Devey, C., Greinert, J., 2016. DeepSurveyCam—a deep ocean optical mapping system. Sensors 16, 164.

Kyuno, A., Shintaku, M., Fujita, Y., Matsumoto, H., Utsumi, M., Watanabe, H., Fujiwara, Y., Miyazaki, J., 2009. Dispersal and differentiation of deep-sea Mussels of the genus Bathymodiolus (Mytilidae, Bathymodiolinae). J. Mar. Biol. 2009, 625672. http://dx.doi.org/10.1155/2009/625672.

Le Dantec, N., Akhtman, Y., Constantin, D., Lemmin, U., Barry, D.A., Pizarro, O., 2013. Morphology of pillow-hollow and quilted-cover bedforms in Lake Geneva, Switzerland. MARID, 15–16.

Luther III, G.W., Rozan, T.F., Taillefert, M., Nuzzio, D.B., Di Meo, C., Shank, T.M., Lutz, R.A., Craig Cary, S., 2001. Chemical speciation drives hydrothermal vent ecology. Nature 410, 813–816.

Mahon, I., Williams, S.B., Pizarro, O., Johnson-Roberson, M., 2008. Efficient view-based SLAM using visual loop closures. IEEE Trans. Robot. 24, 1002–1014.

Marks, R., Rock, S., Lee, M., 1995. Real-time video mosaicking of the ocean floor. IEEE J. Ocean Eng. 20, 229–241.

Marsh, L., Copley, J.T., Huvenne, V.A.I., Tyler, P.A., 2013. Getting the bigger picture: using precision remotely operated vehicle (ROV) videography to acquire high-definition mosaic images of newly discovered hydrothermal vents in the Southern Ocean. Deep Sea Res. II 92, 124–135.

Marsh, L., Copley, J.T., Huvenne, V.A.I., Linse, K., Reid, W.D.K., Rogers, A.D., Sweeting, C.J., Tyler, P.A., 2012. Microdistribution of faunal assemblages at deep-sea hydrothermal vents in the Southern Ocean. PLoS One 7 (10), e48348. http://dx.doi.org/10.1371/journal.pone.0048348.

Massot-Campos, M., Oliver-Codina, G., 2015. Optical sensors and methods for underwater 3D reconstruction. Sensors 15, 31525–31557.

McCollom, T.M., Shock, E.L., 1997. Geochemical constraints on chemolithoautotrophic metabolism by microorganisms in deep-sea hydrothermal systems. Geochim. Cosmochim. Acta 61, 4375–4391.

Moore, K., Jaffe, J.S., 2002. Time-evolution of high-resolution topographic measurements of the sea floor using a 3-D laser line scan mapping system. IEEE J. Ocean Eng. 27, 525–545.

Nakajima, R., Yamakita, T., Watanabe, H., Fujikura, K., Tanaka, K., Yamamoto, H., Shirayama, Y., 2014. Species richness and community structure of benthic macrofauna and megafauna in the deep-sea chemosynthetic ecosystems around the Japanese archipelago: an attempt to identify priority areas for conservation. Divers. Distrib. 20, 1160–1172.

Nakajima, R., Yamamoto, H., Kawagucci, S., Takaya, Y., Nozaki, T., Chen, C., Fujikura, K., Miwa, T., Takai, K., 2015. Post-drilling changes in seabed landscape and megabenthos in a deep-sea hydrothermal system, the Iheya North field, Okinawa Trough. PLoS One 10, 0123095.

Nakamura, K., Takai, K., 2014. Theoretical constraints of physical and chemical properties of hydrothermal fluids on variations in chemolithotrophic microbial communities in seafloor hydrothermal systems. Prog. Earth Planet Sci. 1, 5.

Nakamura, K., Takai, K., 2015. Geochemical constraints on potential biomass sustained by subseafloor water–rock interactions, In: Ishibashi, J., Okino, K., Sunamura, M., (Eds.), Subseafloor Biosphere Linked to Hydrothermal Systems, pp. 11–30.

Negahdaripour, S., Madjidi, H., 2003. Stereovision imaging on submersible platforms for 3-D mapping of benthic habitats and sea-floor structures. IEEE J. Ocean Eng. 28, 625–650.

Nicosevici, T., Gracias, N., Negahdaripour, S., Garcia, R., 2009. Efficient three-dimensional scene modeling and mosaicing. J. Field Robot. 26, 759–788.

Palterson, R., 1975. Future developments in deep-sea imaging. Oceanus 18, 17–23.

Picard, R.R., Cook, R.D., 1984. Cross-validation of regression models. J. Am. Stat. Assoc. 79, 575–583.

Pizarro, O., Singh, H., 2003. Toward large-area mosaicing for underwater scientific applications. IEEE J. Ocean Eng. 28, 651–672.

Pizarro, O., Eustice, R., Singh, H., 2009. Large area 3-d reconstructions from underwater optical surveys. IEEE J. Ocean Eng. 34, 150–169.

Podowski, E.L., Moore, T.S., Zelnio, K.A., Luther III, G.W., Fisher, C.R., 2009. Distribution of diffuse flow mega fauna in two sites on the Eastern Lau Spreading Center, Tonga. Deep Sea Res. I 56, 2041–2056.

Podowski, E.L., Mab, S., Luther III, G.W., Wardrop, D., Fisher, C.R., 2010. Biotic and abiotic factors affecting distributions of megafauna in diffuse flow on andesite and basalt along the Eastern Lau Spreading Center, Tonga. Mar. Ecol. Prog. Ser. 418, 25–45.

Rona, P.A., Klinkhammer, G., Nelsen, T.A., Trefry, J.H., Elderfield, H., 1986. Black smokers, massive sulphides and vent biota at the Mid-Atlantic Ridge. Nature 321, 33–37.

Sarrazin, J., Juniper, S.K., Massoth, G., Legendre, P., 1999. Physical and chemical factors influencing species distributions on hydrothermal sulfide edifices of the Juan de Fuca Ridge, northeast Pacific. Mar. Ecol. Prog. Ser. 190, 89–112.

Sasaki, T., Okutani, T., Fujikura, K., 2005. Molluscs from hydrothermal vents and cold seeps in Japan: a review of taxa recorded in twenty recent years (1984–2004). Venus 64, 87–133.

Sasaki, T., Warén, A., Kano, Y., Okutani, T., Fujikura, K., 2010. Gastropods from recent hot vents and cold seeps: systematics, diversity and life strategies. The Vent and Seep Biota - Aspects from Microbes to Ecosystems 33. Springer, Dordrecht, Netherlands, pp. 169–254 (Topics in Geobiology).

Sen, A., Becker, E.L., Podowski, E.L., Wickes, L.N., Ma, S., Mullaugh, K.M., Hourdez, S., Luther III, G.W., Wickes, C.R., 2013. Distribution of mega fauna on sulfide edifices on the Eastern Lau Spreading Center and Valu Fa Ridge. Deep Sea Res. I 72, 48–60.

Sen, A., Podowski, E.L., Becker, E.L., Shearer, E.A., Gartman, A., Yücel, M., Hourdez, S., Luther III, G.W., Fisher, C.R., 2014. Community succession in hydrothermal vent habitats of the Eastern Lau Spreading Center and Valu Fa Ridge, Tonga. Limnol. Oceanogr. 59, 1510–1528. http://dx.doi.org/10.4319/lo.2014.59.5.1510.

Shank, T.M., Fornari, D.J., Von Damm, K.L., Lilley, M.D., Haymon, R.M., Lutz, R.A., 1998. Temporal and spatial patterns of biological community development at nascent deep-sea hydrothermal vents (9°50′N, East Pacific Rise). Deep Sea Res. Part II 45, 465–515.

Spiess, F.N., Macdonald, K.C., Atwater, T., Ballard, R., Carranza, A., Cordoba, D., Cox, C., Diaz Garcia, V.M., Francheteau, J., Guerrero, J., Hawkins, J., Haymon, R., Hessler, R., Juteau, T., Kastner, M., Larson, R., Luyendyk, B., Macdougall, J.D., Miller, S., Normark, W., Orcutt, J., Rangin, C., 1980. East Pacific rise: hot springs and geophysical experiments. Science 207, 1421–1433.

Takai, K., Mottl, M.J., Nielsen, S.H., 2012. IODP expedition 331: strong and expansive subseafloor hydrothermal activities in the Okinawa Trough. Sci. Drill 13, 19–27.

Takai, K., Mottl, M.J., Nielsen, S.H., the Expedition 331 Scientists, 2011. In: Proceedings of the Integrated Ocean Drilling Program 331. Integr. Ocean Drill Program Manage Int., Tokyo. doi: ⟨http://dx.doi.org/10.2204/iodp.proc.331.2011http://dx.doi.org/10.2204/iodp.proc.331.2011⟩.

Thornton, B., Sakka, S., Takahashi, T., Takumi, S., Ohki, T., Ohki, K., 2015. Development of a deep-sea laser induced breakdown spectrometer for in situ multi-element chemical analysis. Deep Sea Res. I 95, 20–36.

Tsuji, T., Takai, K., Oiwane, H., Nakamura, Y., Masaki, Y., Kumagai, H., Kinoshita, M., Yamamoto, F., Okano, T., Kuramoto, S., 2012. Hydrothermal fluid flow system around the Iheya North Knoll in the mid-Okinawa trough based on seismic reflection data. J. Volcanol. Geotherm. Res. 213–214, 41–50.

Van Dover, C.L., 2014. Impacts of anthropogenic disturbances at deep-sea hydrothermal vent ecosystems: a review. Mar. Environ. Res. 102, 59–72.

Van Dover, C.L., German, C.R., Speer, K.G., Parson, L.M., Vrijenhoek, R.C., 2002. Evolution and biogeography of deep-sea vent and seep invertebrates. Science 295, 1253–1257.

Watanabe, H., Kojima, S., 2015. Vent Fauna in the Okinawa Trough. In: Isibashi, J., Okino, K., Sunamura, M. (Eds.), Subseafloor Biosphere Linked to Hydrothermal Systems: TAIGA Concept. Springer, Japan, pp. 449–459.

Watanabe H., Fujikura K., Kojima S., Miyazaki J., Fujiwara, Y., Japan: Vents and Seeps in Close Proximity, In: The Vent and Seep Biota – Aspects from Microbes to Ecosystems 33, 2010, Springer; Dordrecht, Netherlands, 379–401, (Topics in Geobiology).

Wiens, J.A., Hayward, G.D., Holthausen, R.S., Wisdom, M.J., 2008. Using surrogate species and groups for conservation planning and management. BioScience 58, 241–252.

Wirsen, C.O., Jannasch, H.W., Molyneaux, S.J., 1993. Chemosynthetic microbial activity at Mid-Altantic Ridge hydrothermal vent sites. J. Geophys. Res. 98, 9693–9703.

Yahagi, T., Watanabe, H., Ishibashi, J., Kojima, S., 2015. Genetic population structure of four hydrothermal vent shrimp species (Alvinocarididae) in the Okinawa Trough, Northwest Pacific. Mar. Ecol. Prog. Ser. 529, 159–169.

Yamanaka, T., Shimamura, S., Nagashio, H., Yamagami, S., Onishi, Y., Hyodo, A., Mampuku, M., Mizota, C., 2015. A Compilation of the stable isotopic compositions of carbon, nitrogen, and sulfur in soft body parts of animals collected from deep-sea hydrothermal vent and methane seep fields: variations in energy source and importance of subsurface microbial processes in the sediment-hosted systems. In: Isibashi, J., Okino, K., Sunamura, M. (Eds.), Subseafloor Biosphere Linked to Hydrothermal Systems: TAIGA Concept. Springer, Japan, pp. 105–129.